Wind Energ. Sci., 11, 2669–2694, 2026
https://doi.org/10.5194/wes-11-2669-2026

WIND ENERGY SCIENCE
Open Access

Large-eddy simulation of airborne wind energy systems flying in turbulent wind using model predictive control

Jean-Baptiste Crismer[1], **Thomas Haas**[2], **Matthieu Duponcheel**[1], **and Grégoire Winckelmans**[1]

[1]Institute of Mechanics, Materials and Civil Engineering (iMMC), Université catholique de Louvain (UCLouvain), 1348 Louvain-la-Neuve, Belgium

[2]Thermodynamics and Fluid Mechanics (FLOW), Faculty of Engineering, Vrije Universiteit Brussel (VUB), 1050 Brussels, Belgium

Correspondence: Jean-Baptiste Crismer (jean-baptiste.crismer@uclouvain.be)

Received: 20 December 2025 – Discussion started: 9 January 2026
Revised: 18 May 2026 – Accepted: 22 May 2026 – Published: 27 July 2026

Abstract. Wind energy is expected to play a key role in the future energy mix, but the increasing size of conventional wind turbines poses growing structural and material challenges. Airborne wind energy (AWE) offers a promising alternative; however, its large-scale deployment requires further studies of airborne wind energy system (AWES) operation under turbulent conditions and within wind farms.

This work proposes a framework based on computational fluid dynamics for studying AWES in ambient turbulent wind and wakes, as will be encountered when arranged in farms. The present work focuses on ground-gen rigid-wing AWESs. The framework relies on a large-eddy simulation flow solver, in which the kites are represented using a model based on an actuator line for the main wing with its ailerons and complemented with models for the tail control surfaces (rudder and elevator). The flow solver is coupled, via a two-way coupling, to a control module based on model predictive control, to follow optimal trajectories. The framework is presented in some detail and is then used to investigate the MegAWES aircraft, a MW-scale AWES of 42.5 m wingspan, here flying four-loop trajectories. The first part of the investigation focuses on a single system. Its ability to fly in a turbulent wind is demonstrated and analyzed, and its wake is also characterized. It is demonstrated that the controlled kite can handle the turbulent wind. The deviation from its reference trajectory is less than 15 % of the wingspan. In the second part of the paper, a tandem configuration is considered, with the same four-loop trajectory for each kite. It is found that there is a configuration where the second kite, even fully aligned with the first one, can fly in unperturbed flow (other than the turbulence of the wind). A second case is investigated where the second kite is forced to fly in the wake from the first one. It is found that the wake produced by the first kite does not compromise the trajectory tracking of the second kite. However, the second kite feels the velocity deficit, and its power production is reduced by 6 %.

1 Introduction

Wind energy is a cornerstone of the energy transition, and significant capacity expansion is expected in the coming decades (IEA – International Energy Agency, 2021). Although horizontal-axis wind turbines (HAWTs) are the most common technology to harness wind energy, scaling limitations have led to growing interest in exploring alternative technologies. Among them, airborne wind energy systems (AWESs) have attracted increasing interest due to their low material use and access to high-altitude winds (Loyd, 1980; Hagen et al., 2023).

Airborne wind energy (AWE) relies on tethered wings, i.e., kites, to harvest energy from the wind. The present work focuses on fixed-wing, lift-based AWES, which is one of the most studied concepts. These are aircraft-type systems for which the generator is on the ground. Its operation consists of repeating pumping cycles with two distinct phases. During

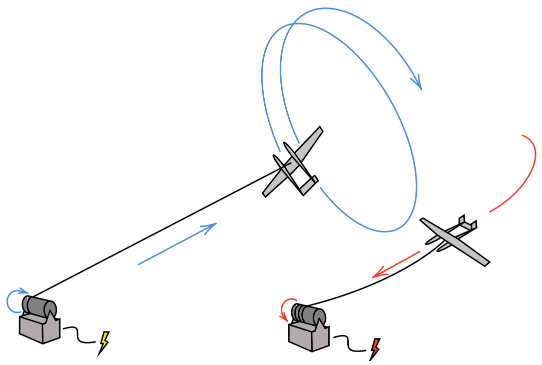

Figure 1. Ground-gen airborne wind energy system operating phases: reel-out (left) and reel-in (right) phases. Inspired by Joshi et al. (2024).

the "reel-out phase", the kite flies crosswind loops and pulls on the tether to drive a generator. In the subsequent "reel-in phase", the kite returns toward the ground station and the tether is rewound onto the drum. The device studied here is the reference rigid-wing AWES proposed by Eijkelhof and Schmehl (2022). The system and its operation are depicted in Fig. 1.

Much of the research conducted on AWESs focuses on control and optimal path generation. Indeed, an AWES can move freely in space within a given set of constraints. The trajectory determines the energy yield of the system and is a first challenge that constitutes a vast research field (Eijkelhof and Schmehl, 2022; De Schutter et al., 2023; Vermillion et al., 2021). The second challenge is the accurate tracking of the computed/optimized trajectory, as it directly affects the system performances. The tracking is even more complex when one considers the flow unsteadiness present in atmospheric flows (such as wind turbulence, wind shear, and gusts). In addition, AWES operation may involve crossing wakes generated by other devices, such as other AWESs when considering a farm of AWESs (Haas et al., 2022) or even a HAWT when considering AWESs added to a farm of HAWTs. Therefore, it is of prime importance to understand how these devices interact with complex and realistic flows. This is a key aspect for the industrial implementation of AWESs and their operation in wind farms.

Studying AWES performance in realistic conditions requires coupled models of the atmospheric flow, the wing aerodynamics, the tether, the ground station, and the flight dynamics, with a trade-off between fidelity and computational cost. This motivates the range of modeling approaches found in the literature, from reduced-order simulators for control design to CFD-based frameworks for wing and/or wake-resolving studies. An overview of the different existing models is established by Vermillion et al. (2021), with a focus on dynamics and control, while Pynaert et al. (2023) propose a first classification of the different fidelity levels for aerodynamics and aero-elasticity.

Most studies focusing on developing kite simulators, or more generally on control and optimal trajectory, opt for simplified aerodynamic models (Sánchez-Arriaga et al., 2019; Eijkelhof and Schmehl, 2022; Rapp et al., 2019; De Schutter et al., 2023). They rely on 6 degrees of freedom (DOF) dynamics models and use stability derivatives models or lookup tables to model the aerodynamic forces. While such models are computationally efficient and often sufficiently accurate for force estimation, they lack accuracy and do not take into account the flow unsteadiness or wakes, which are key aspects for realistic operation.

Although more complex aerodynamic models for rigid-wing AWESs exist, studies are still quite scarce, and only a few combine control capabilities with unsteady flow and wake modeling. One of the most advanced works with respect to these aspects is the work of Pynaert et al. (2024) who developed a whole aero-servo framework using wing-resolved unsteady RANS (URANS) simulations. However, URANS approaches are known to have limitations in accurately resolving turbulence structures and wake dynamics. Haas et al. (2022) proposed an LES-based framework that combines actuator-based AWES representation, model-based trajectory optimization, and closed-loop optimal control. In their approach, the atmospheric boundary layer (ABL) flow is resolved using large-eddy simulation (LES), while the kite's wing is represented using an actuator sector method (ASM). The ASM is less accurate than a resolved wing. Nonetheless, it uses LES to represent the flow, which provides an accurate representation of turbulence and wakes. The system dynamics is modeled with a 3-DOF point-mass model. With this model, flight path optimization and closed-loop control by means of non-linear model predictive control (NMPC) are performed using the optimal control toolbox `AWEbox` (De Schutter et al., 2023). This framework enables the study of wake interactions in turbulent wind conditions, providing valuable insights into AWES performance at the farm scale. While highly effective, this approach uses reduced-order dynamics, which does not resolve the kite rotational motion. Also, the ASM is a simplified variant of the actuator line method that considers a temporally weighted influence of the AWES on the flow. The coupling between the actuator method and the dynamics is also simplified: aerodynamic forces are computed using a separate reduced model that takes as input the velocity sampled from the ASM, rather than using the forces directly evaluated by the ASM. To the best of the authors' knowledge, no previous study combines LES-resolved atmospheric turbulence with a 6-DOF dynamics model and actuator line aerodynamic representation including control surfaces within a closed-loop control framework.

The present work therefore introduces an LES-based aero-servo simulation framework similar to Haas et al. (2022) but employing refined models for the system dynamics and aerodynamics. To this end, the kite dynamics are represented using a 6-DOF model, while the wing aerodynamics are described using an actuator line (AL) approach. To compute the aerodynamic moments required by the 6-DOF model, the influence of the control surfaces is incorporated into the AL representation of the main wing. This results in a complete aircraft model. The control surface models are based on their geometry and lift slope coefficient. A two-way coupling between the AL-based model and the NMPC module of AWEbox allows closed-loop control flight simulations. Here, the system motion is therefore driven by the aerodynamic forces directly obtained from the AL-based model in the LES. The kite trajectories are generated with AWEbox. The framework is subsequently utilized to compare system performances between idealized conditions in AWEbox and turbulent wind conditions.

This paper builds upon previous work (Crismer et al., 2024), further detailing the framework developed and extending it to more realistic trajectories. Furthermore, the framework is used to investigate the case of a single kite and the case of two kites in tandem, where the second one flies just behind the first one.

The tools and building blocks of the framework are presented in Sect. 2. A study of the AL accuracy is reported in Sect. 3. Section 4 details the numerical setup and the parameters used. The results obtained for the different investigated cases are presented and discussed in Sect. 5. Finally, conclusions are presented in Sect. 6.

2 Methodology

This section presents the different components of the framework. The flow solver is first introduced in Sect. 2.1. The system dynamics are described in Sect. 2.2. Section 2.3 presents the tether model used in this work, as implemented in AWEbox. The aircraft model is then discussed in Sect. 2.4. Finally, Sect. 2.5 covers AWEbox, which is used for trajectory generation and control.

2.1 Flow solver

An LES approach combined with realistic modeling of the AWES (using an improved AL method for the wing and added modeling of the control surfaces: ailerons, rudder, and elevator) is used here. We use LES because it allows for an accurate modeling of the flow turbulence and unsteadiness, and is therefore well suited to represent realistic wind.

The LES solver is based on fourth-order finite-differences for incompressible flows. It was developed at UCLouvain (Duponcheel et al., 2014; Moens and Chatelain, 2022). The Navier–Stokes equations are solved in their velocity-pressure formulation, truncated by the LES grid size, and supplemented with a subgrid-scale (SGS) model:

$$\nabla \cdot \boldsymbol{v} = 0 \tag{1a}$$

$$\frac{\partial \boldsymbol{v}}{\partial t} + (\boldsymbol{v} \cdot \nabla)\boldsymbol{v} = -\nabla P + \nu \nabla^2 \boldsymbol{v} + \nabla \cdot \tau^{\mathrm{SGS}} + \boldsymbol{f}, \tag{1b}$$

where $\boldsymbol{v}$ is the velocity field, t is the time, $P = p/\rho$ is the kinematic pressure field, and $\nu = \mu/\rho$ is the kinematic viscosity of the fluid. τ^{SGS} is the SGS stress tensor (also divided by ρ). It is modeled using the regularized variational multiscale (RVM) model (Jeanmart and Winckelmans, 2007; Cocle et al., 2009). The volumetric forcing term $\boldsymbol{f}$ is used to represent the effect of AWESs. The domain is discretized using a Cartesian staggered grid. The temporal integration is handled using the second-order Adams–Bashforth scheme.

The turbulent inflow consists of either synthetic turbulent fluctuations generated using the Mann algorithm (Mann, 1994) and added to the mean wind, or a neutral atmospheric boundary layer (ABL) obtained using a co-simulation (Trigaux et al., 2024a; Moens and Chatelain, 2022).

We stress that the LES solver, combined with improved AL modeling, has already been used in previous studies relating to wind energy. For instance, it was used to investigate the blade flexibility effects on the loads and wake of the very large IEA 15 MW horizontal-axis wind turbine in Trigaux et al. (2024a). The investigations included both cases of turbulent wind, using a Mann box (hence no mean shear) and using an ABL running as a LES co-simulation (hence also with mean wind shear).

The present study focuses on the ability of the kite and its controller to maintain stable flight in turbulent flows and under external perturbations, such as the wake of another kite. To isolate the turbulence and wake effects, it is chosen to consider a uniform mean inflow and synthetic turbulence using Mann boxes pre-generated with Hipersim (Dimitrov et al., 2024).

2.2 AWES dynamics

When the kite flies with the controller, the dynamics are handled using the dynamics model from AWEbox (De Schutter et al., 2023), which is a modeling and optimization toolbox for AWESs. The AWES can be decomposed into three main components: the ground station, which hosts the generator; the tether; and the kite. In the system model, the ground station is not modeled and the kite is directly controlled using the tether jerk (third derivative of the tether length). The tether is assumed to be a straight rod of varying length, going from the ground station to the kite center of gravity (CG) and subjected to drag only. Finally, the kite itself is modeled using a 6-DOF model for its dynamics, subject to forces and moments. The computation of the forces and moments is handled using the actuator line and the control surfaces models within the flow solver, as presented in Sect. 2.4.

Two coordinate systems come into play to describe the system dynamics. The origin of the inertial coordinate system is placed at the ground station with the x axis in the flow direction, the z axis pointing upward, and the y axis sideways to form a right-hand coordinate system. The body coordinate system origin is located at the CG of the kite, with the x axis pointing backward, the y axis pointing star-

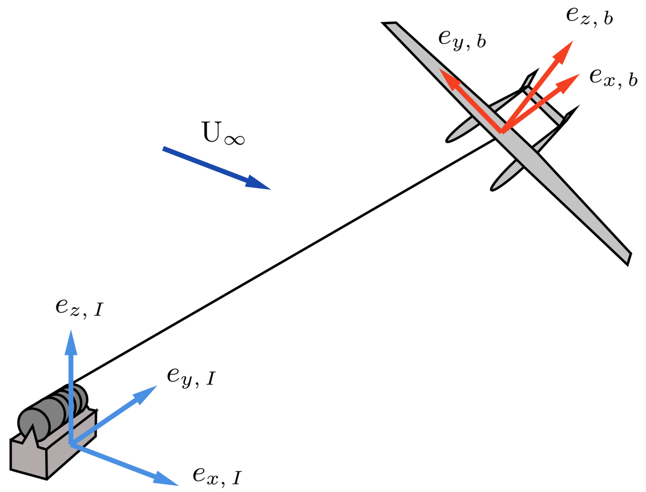

Figure 2. The airborne wind energy system and the reference frames.

board, and the z axis pointing upward, as shown in Fig. 2. The kite position in the inertial frame is described by its coordinates $\boldsymbol{q}$. The orientation of the kite in this reference frame is represented using a rotation matrix $\mathbf{R} \triangleq [\boldsymbol{e}_{x,b}; \boldsymbol{e}_{y,b}; \boldsymbol{e}_{z,b}]^{\mathrm{T}}$ that contains chord-wise, spanwise, and upwards unit vectors of the aircraft body frames, expressed in the inertial frame $\{\boldsymbol{e}_{x,I}; \boldsymbol{e}_{y,I}; \boldsymbol{e}_{z,I}\}$, and transforms the different vectors from the inertial frame to the kite body frame.

The kite state vector is the concatenation of the kite position $\boldsymbol{q}$; translational velocity $\dot{\boldsymbol{q}}$; rotational velocity $\boldsymbol{\omega}$; orientation described by the rotation matrix $\mathbf{R}$, control surfaces deflection $\boldsymbol{\delta}$, which is the concatenation of $[\delta_{\mathrm{a}}; \delta_e; \delta_r]$ (ailerons, elevator, and rudders actuation angles, respectively) and the tether length l, tether velocity $\dot{l}$, and tether acceleration $\ddot{l}$; and is therefore defined as

$$\boldsymbol{x} \triangleq \left(\boldsymbol{q}, \dot{\boldsymbol{q}}, \boldsymbol{\omega}, \mathbf{R}, \boldsymbol{\delta}, l, \dot{l}, \ddot{l}\right). \tag{2}$$

The control variables of the system are contained in the vector

$$\boldsymbol{u} \triangleq \left(\dot{\boldsymbol{\delta}}, \dddot{l}\right), \tag{3}$$

and is a concatenation of the control surfaces actuation rates and the tether jerk.

The equations of motion of the kite are derived from Lagrangian mechanics (Gros and Diehl, 2013; De Schutter et al., 2023), expressed as

$$m\,\ddot{\boldsymbol{q}} - \lambda\,\boldsymbol{q} = \mathbf{R}^{\mathrm{T}}\boldsymbol{F}_{e,b} - \overline{m}\,g\,\boldsymbol{e}_{z,I} \tag{4a}$$

$$\ddot{c} + 2\kappa_t\,\dot{c} + \kappa_t^2\,c = 0 \tag{4b}$$

$$\mathbf{J}\,\dot{\boldsymbol{\omega}} + \boldsymbol{\omega} \times \mathbf{J}\boldsymbol{\omega} = \boldsymbol{M}_{e,b} \tag{4c}$$

$$\frac{\mathrm{d}}{\mathrm{d}t}\mathbf{R} = \mathbf{R}\left(\frac{\kappa_R}{2}\left(I - \mathbf{R}^{\mathrm{T}}\mathbf{R}\right) - \mathtt{skew}(\boldsymbol{\omega})\right). \tag{4d}$$

Equation (4a) corresponds to the translational kinematics, in which $m = (m_K + \frac{1}{3}m_T)$ and $\overline{m} = (m_K + \frac{1}{2}m_T)$ are the effective inertial and effective gravitational masses (Houska and Diehl, 2007) (with m_K and m_T the mass of the kite and of the tether, respectively), $\boldsymbol{F}_{e,b}$ is the external forces expressed in the body frame, g is the gravitational acceleration, and λ is the Lagrangian multiplier inherent to the chosen formulation. The translational kinematics is constrained with Eq. (4b), in which $c = \frac{1}{2}(\boldsymbol{q}^{\mathrm{T}}\boldsymbol{q} - l^2) = 0$ is the constraints that forces the kite to navigate on a hemisphere of radius equal to the tether length; and κ_t is a constant stabilizing parameter. It is the Baumgarte stabilized form of the latter constraint c. Equation (4c) refers to the rotational kinematics, in which $\mathbf{J}$ is the kite inertia matrix, and $\boldsymbol{M}_{e,b}$ is the external moments. A similar stabilization is used to guarantee the orthogonality of the rotation matrix. Equation (4d) both describes the evolution of the rotation matrix and guarantees its orthogonality $\boldsymbol{c}_R = \mathbf{R}^{\mathrm{T}}\mathbf{R} - I = 0$. In this equation, κ_t is another constant stabilizing parameter, and `skew` is an operator that transforms a vector into the corresponding skew-symmetric matrix. Such stabilization also requires the initial constraint $C(\boldsymbol{x_0}) = (c(\boldsymbol{x_0}), \dot{c}(\boldsymbol{x_0}), \boldsymbol{c}_R(\boldsymbol{x_0})) = 0$. The interested reader can find more details on the dynamics formulation in Gros and Diehl (2013) and De Schutter et al. (2023).

The system dynamics are integrated in time using a 4th order Runge–Kutta scheme:

$$\dot{\boldsymbol{x}} = \frac{\mathrm{d}\boldsymbol{x}}{\mathrm{d}t} = \left(\dot{\boldsymbol{q}}, \ddot{\boldsymbol{q}}, \dot{\boldsymbol{\omega}}, \dot{\mathbf{R}}, \dot{\boldsymbol{\delta}}, \dot{l}, \ddot{l}, \dddot{l}\right). \tag{5}$$

The external forces $\boldsymbol{F}_{e,I} = \mathbf{R}^{\mathrm{T}}\boldsymbol{F}_{e,b}$ applied to the system are the aerodynamic forces. The aerodynamic forces consist of the aerodynamic forces acting on the kite and the tether drag. Their evaluation is described in the following sections.

2.3 Tether model

The tether drag is evaluated assuming the drag coefficient $C_{D,T} = 1.2$ for a circular cross-section. The total drag on the tether is shared between the ground station and the kite, as detailed in De Schutter et al. (2023). The contribution that acts on the kite is evaluated by integrating along the tether using the coordinate $s \in [0, 1]$. An infinitesimal tether fragment therefore has a length of $dl = l\,ds$, and the integral writes

$$\boldsymbol{F}_{D_T} = \int_0^1 s\left(\frac{1}{2}\rho \parallel \boldsymbol{v}_{\mathrm{a},t}(s) \parallel \boldsymbol{v}_{\mathrm{a},t}(s)\,C_{D,T}\,d_T\right)(l\,\mathrm{d}s), \tag{6}$$

where $\boldsymbol{v}_{\mathrm{a},t}(s)$ is the apparent velocity projected perpendicularly to the tether and d_T is the tether diameter. The weighting factor s specifies the fraction of the total drag attributed to the kite. For each infinitesimal tether element, the drag is partitioned between the ground station and the kite according to its position along the tether: a weight of $(1 - s)$ applies to the ground station, and a weight of s applies to the kite. The other part acts on the ground station. The integration is required because the drag force is not constant along the tether, as the apparent velocity varies along its length. In AWEbox, the integration is performed numerically by dividing the tether into n elements. Here, $n = 5$.

2.4 Kite AL model and models for the effect of the control surfaces

The aerodynamic forces that act on the kite are taken from the flow solver AL model. In this model, the main wing of the kite is modeled using an actuator line (AL) model, as in Sørensen and Shen (2002), and that line is immersed in the flow solver, meaning that it moves relative to the fixed Cartesian grid of the flow solver.

Capturing the effects of the turbulence on the kite requires that the flow solver grid size be sufficiently fine relative to the wingspan of the kite. It must therefore be sufficiently fine everywhere in the region of the flow domain through which the kite moves.

The AL method involves three main steps: flow velocity sampling, forces and moments evaluation, and forces projection into the fluid. The AL is discretized into N segments, with a control point at the center of each segment. These control points are used as reference locations for the three main operations of the method. Knowing the position and orientation of the wing, the AL is placed along the quarter-chord line, and the positions of the control points are determined. For each control point, the local flow velocity is evaluated by performing a weighted average of the flow velocity in the vicinity of the control point. Once the velocity is known, the aerodynamic forces and moments are computed on the basis of airfoil polar data. Finally, the forces are projected onto the mesh surrounding the corresponding control point. They are accounted for by the flow solver through the volumetric force term on the right-hand side of Eq. (1b). Velocity sampling and force distribution are performed by means of a 2D Gaussian regularization kernel. Indeed, 2D kernels have been shown to be more accurate in predicting aerodynamic forces than the 3D kernel (Caprace et al., 2020). In practice, a planar grid with its associated weights, referred to as a template, is placed at each control point, perpendicular to the AL. Linear interpolation is then used to transfer information from the template to the flow solver grid, and vice versa. More details on the implementation of the AL method can be found in Trigaux et al. (2024a, b).

This work considers the rigid-wing reference AWES, called MegAWES (Eijkelhof and Schmehl, 2022). It has a wingspan of 42.5 m and a main wing aspect ratio of 12. The complete geometry considered in the present work is detailed in Appendix A. The geometry is slightly adapted to solve inconsistencies and simplify some parts.

The aircraft has two ailerons on the wing, one elevator, and two rudders. Their associated quantities are denoted with the subscripts a, e, and r, respectively. They are modeled as flat plates hinged about their aerodynamic center (i.e., at their quarter chord). Owing to their low aspect ratio, these control surfaces are not well suited for an AL representation. Moreover, their dimensions are small relative to affordable grid resolution of the flow solver, which prevents an adequate spatial discretization. Their force contribution is therefore modeled analytically as ($\diamond \in [e, r]$)

$$L_\diamond = \frac{1}{2}\rho \parallel \boldsymbol{v}_{\mathrm{a},\diamond} \|^2 A \frac{\mathrm{d}C_L}{\mathrm{d}\alpha}|_\diamond \alpha_\diamond, \tag{7}$$

where A is the control surface area, $\frac{\mathrm{d}C_L}{\mathrm{d}\alpha}|_\diamond$ is its effective lift slope coefficient, and $\alpha_\diamond$ is the angle of attack of the measured apparent velocity relative to the chord. The lift slope coefficients were evaluated using a lifting surface method, thus properly taking into account the low aspect ratio of the control surface and the wake vorticity produced by it. As these estimates closely match those obtained from the Helmbold approximation for low-aspect-ratio wings, the latter is adopted, yielding values of $\frac{\mathrm{d}C_L}{\mathrm{d}\alpha}|_e = 1.01\pi$ for the elevator and $\frac{\mathrm{d}C_L}{\mathrm{d}\alpha}|_r = 0.50\pi$ for the rudders.

The apparent velocity $\boldsymbol{v}_{\mathrm{a},\diamond}$ is obtained from the kite velocity and the local flow velocity. The flow velocity is interpolated at the aerodynamic center of each control surface using an $M'4$ kernel (Monaghan, 1985). The resulting aerodynamic loads are added to the forces acting on the body, with the resulting moments. Because these loads are small compared to those generated by the main wing, their impact on the flow field is neglected (i.e., we neglect the small wake vortices that they produce), and their influence is restricted to the body dynamics.

Aileron effects are incorporated directly within the actuator line framework by adjusting the local airfoil characteristics according to the aileron deflection angle δ_a. For the ith wing section of chord c_i, the lift per unit span is expressed as

$$l_i(\alpha) = \frac{1}{2}\rho \parallel \boldsymbol{v}_{\mathrm{a},i} \|^2 c_i \left(C_l(\alpha) + p_i \left((\eta\,\tau) \frac{\mathrm{d}C_l}{\mathrm{d}\alpha}|_\mathrm{a} \delta_\mathrm{a} \right) \right), \tag{8}$$

where τ is the aileron effectiveness factor which depends on the fraction of the chord spanned by the aileron c_a/c_i and $\eta = \eta(\delta_\mathrm{a}) < 1$ is a correction factor to account for the reduced aileron effectiveness as the deflection angle increases – see McCormick (1995). In this case, $c_a/c_i = 0.25$ and $\tau = 0.6$. The lift slope of the ailerons $\frac{\mathrm{d}C_l}{\mathrm{d}\alpha}|_\mathrm{a}$ is that of the aerodynamic profile at its zero-lift angle. The contribution of an aileron to an AL control point is weighted proportionally to the fraction p_i that it spans on that AL segment. The influence of the ailerons is thus taken into account in the computation of the force distribution over the wing. A schematic of the whole AL-based kite model is depicted in Fig. 3.

It should be noted that, due to the variation of the wing properties (chord, twist, presence of ailerons), the number of AL control points must be chosen so that it can capture those characteristics.

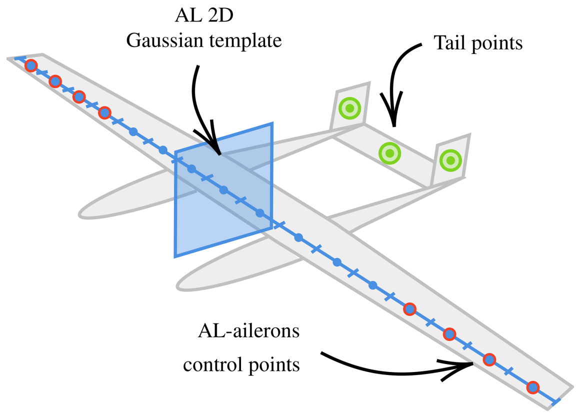

Figure 3. Schematic of the kite model with the actuator line model, including the ailerons, for the main wing, and the evaluation points for the elevator and rudders models.

2.5 Reference trajectories and control

The power output of an AWES is determined by its trajectory. It also depends on how well the kite can follow the planned trajectory. In the present work, the kite flies so-called "optimal trajectories" in the sense that the reference trajectories are generated through an optimization process performed using `AWEbox` (De Schutter et al., 2023). This is presented in Sect. 2.5.1. The controller is then used to fly these pre-computed optimal trajectories in the turbulent wind using flight path tracking. The control strategy is introduced in Sect. 2.5.2.

2.5.1 Optimal trajectories

`AWEbox` generates optimal trajectories by solving optimal control problems (OCPs). In this case, we want to find a reference trajectory for the following optimization variables: the states $\boldsymbol{x}(t)$, the control input $\boldsymbol{u}(t)$, the algebraic variable $z(t) = \lambda$, a set of system constant parameters $\boldsymbol{p}$, and the trajectory time period T_p. Note that some system design parameters can also be optimized, such as the tether diameter; in our case, it is prescribed as a system parameter.

The trajectory is to be optimized so that it minimizes a cost function over the trajectory period. It takes into account the total power output, as well as a penalty on the use of the actuators $\boldsymbol{u}(t)$, side-slip $\beta(t)$, and angular acceleration $\dot{\boldsymbol{\omega}}(t)$, in order to prevent actuator fatigue and aggressive maneuvers. The penalty function $\hat{\boldsymbol{w}}(t) \triangleq [\boldsymbol{u}(t), \beta(t), \dot{\boldsymbol{\omega}}(t)]$ is associated with weights $\mathbf{W}$. The optimization is constrained by the system dynamics, as described in Sect. 2.2 and summarized as

$$\boldsymbol{F}\left(\dot{\boldsymbol{x}}(t), \boldsymbol{x}(t), \boldsymbol{u}(t), z(t), \boldsymbol{p}\right) = 0, \tag{9}$$

and a set of constraints $\boldsymbol{h}$ that ensures that the system operation remains within acceptable bounds to preserve the hardware. The trajectory must also remain periodic, and the whole problem therefore reads

$$\min_{\boldsymbol{x}(t),\boldsymbol{u}(t),\lambda(t),T_\mathrm{p}} \frac{1}{T_\mathrm{p}} \int_0^{T_\mathrm{p}} \left(-P(t) + \hat{\boldsymbol{w}}(t)^\mathrm{T} \mathbf{W} \hat{\boldsymbol{w}}(t)\right) \mathrm{d}t \tag{10a}$$

$$\text{s.t. } \boldsymbol{F}\left(\dot{\boldsymbol{x}}(t), \boldsymbol{x}(t), \boldsymbol{u}(t), \lambda(t), \boldsymbol{p}\right) = 0, \forall t \in [0, T_\mathrm{p}] \tag{10b}$$

$$\boldsymbol{h}\left(\dot{\boldsymbol{x}}(t), \boldsymbol{x}(t), \boldsymbol{u}(t), \lambda(t), \boldsymbol{p}\right) \leq 0, \forall t \in [0, T_\mathrm{p}] \tag{10c}$$

$$\boldsymbol{x}(0) - \boldsymbol{x}(T_\mathrm{p}) = 0. \tag{10d}$$

For the optimization, the aerodynamic forces and moments must be given in the form of analytical expressions. The simplified internal aerodynamic model (Malz et al., 2019) is used and is formulated as follows:

$$\boldsymbol{F}_\mathrm{a} = \frac{1}{2}\rho \|\boldsymbol{v}_a\|^2 S \begin{bmatrix} C_x\left(\alpha, \beta, \boldsymbol{\omega}, \delta_{\mathrm{a},e,r}\right) \\ C_y\left(\alpha, \beta, \boldsymbol{\omega}, \delta_{\mathrm{a},e,r}\right) \\ C_z\left(\alpha, \beta, \boldsymbol{\omega}, \delta_{\mathrm{a},e,r}\right) \end{bmatrix},$$

$$\boldsymbol{M}_a = \frac{1}{2}\rho \|\boldsymbol{v}_a\|^2 S \begin{bmatrix} b\,C_l\left(\alpha, \beta, \boldsymbol{\omega}, \delta_{\mathrm{a},e,r}\right) \\ \bar{c}\,C_m\left(\alpha, \beta, \boldsymbol{\omega}, \delta_{\mathrm{a},e,r}\right) \\ b\,C_n\left(\alpha, \beta, \boldsymbol{\omega}, \delta_{\mathrm{a},e,r}\right) \end{bmatrix}, \tag{11}$$

where S is the wing surface, $\boldsymbol{v}_a$ is the apparent wind velocity, α is the aircraft angle of attack, and β its side-slip angle (all measured at CG). The associated sub-coefficients are

$$\begin{aligned} \begin{bmatrix} C_x \\ C_y \\ C_z \end{bmatrix} &= \begin{bmatrix} C_{x_0} \\ C_{y_0} \\ C_{z_0} \end{bmatrix} + \begin{bmatrix} C_{x_\beta} \\ C_{y_\beta} \\ C_{z_\beta} \end{bmatrix} \beta \\ &+ \begin{bmatrix} C_{x_{\omega_x}} & C_{x_{\omega_y}} & C_{x_{\omega_z}} \\ C_{y_{\omega_x}} & C_{y_{\omega_y}} & C_{y_{\omega_z}} \\ C_{z_{\omega_x}} & C_{z_{\omega_y}} & C_{z_{\omega_z}} \end{bmatrix} \begin{bmatrix} b\,\omega_x \\ \bar{c}\,\omega_y \\ b\,\omega_z \end{bmatrix} \frac{1}{2\|\boldsymbol{v}_a\|^2} + \begin{bmatrix} C_{x_{\delta_\mathrm{a}}} \\ C_{y_{\delta_\mathrm{a}}} \\ C_{z_{\delta_\mathrm{a}}} \end{bmatrix} \delta_\mathrm{a} \\ &+ \begin{bmatrix} C_{x_{\delta_e}} \\ C_{y_{\delta_e}} \\ C_{z_{\delta_e}} \end{bmatrix} \delta_e + \begin{bmatrix} C_{x_{\delta_r}} \\ C_{y_{\delta_r}} \\ C_{z_{\delta_r}} \end{bmatrix} \delta_r \end{aligned} \tag{12a}$$

$$\begin{aligned} \begin{bmatrix} C_l \\ C_m \\ C_n \end{bmatrix} &= \begin{bmatrix} C_{l_0} \\ C_{m_0} \\ C_{n_0} \end{bmatrix} + \begin{bmatrix} C_{l_\beta} \\ C_{m_\beta} \\ C_{n_\beta} \end{bmatrix} \beta \\ &+ \begin{bmatrix} C_{l_{\omega_x}} & C_{l_{\omega_y}} & C_{l_{\omega_z}} \\ C_{m_{\omega_x}} & C_{m_{\omega_y}} & C_{m_{\omega_z}} \\ C_{n_{\omega_x}} & C_{n_{\omega_y}} & C_{n_{\omega_z}} \end{bmatrix} \begin{bmatrix} b\,\omega_x \\ \bar{c}\,\omega_y \\ b\,\omega_z \end{bmatrix} \frac{1}{2\|\boldsymbol{v}_a\|^2} + \begin{bmatrix} C_{l_{\delta_\mathrm{a}}} \\ C_{m_{\delta_\mathrm{a}}} \\ C_{n_{\delta_\mathrm{a}}} \end{bmatrix} \delta_\mathrm{a} \\ &+ \begin{bmatrix} C_{l_{\delta_e}} \\ C_{m_{\delta_e}} \\ C_{n_{\delta_e}} \end{bmatrix} \delta_e + \begin{bmatrix} C_{l_{\delta_r}} \\ C_{m_{\delta_r}} \\ C_{n_{\delta_r}} \end{bmatrix} \delta_r, \end{aligned} \tag{12b}$$

where b is the wingspan and $\bar{c} = S/b$ its mean chord. Each coefficient $C_{\_,\_}$ of Eqs. (12a) and (12b) is modeled using a second-order polynomial that depends on the angle of attack α. Those sub-coefficients were evaluated using the whole AL kite model and imposing the corresponding displacement or actuation. More details are provided in Appendix C.

2.5.2 Control strategy

The kite flies the generated trajectory in a turbulent environment emulated by the LES. To guarantee that the kite stays on the desired trajectory, it has to be associated with a controller. In AWEbox, the flight path tracking is performed using non-linear model predictive control (NMPC). The model is the same as that used for trajectory optimization, as described in previous sections. At each call of the controller, for a given state $\boldsymbol{x}_i$ and knowing the reference trajectory $\boldsymbol{x}_{\mathrm{ref}}$, the controller computes the best possible control actions in order to stick to the reference path. The prediction is done for a given time horizon T_{h}, starting at the current simulation time t_{s}. For each prediction, an OCP is formulated (Zanon et al., 2013):

$$\min_{\boldsymbol{x}(t),\boldsymbol{u}(t),z(t)} \int_{t_{\mathrm{s}}}^{t_{\mathrm{s}}+T_{\mathrm{h}}} \left(\|\boldsymbol{x}(t)-\boldsymbol{x}_{\mathrm{ref}}(t)\|^2_{Q_C} + \|\boldsymbol{u}(t)-\boldsymbol{u}_{\mathrm{ref}}(t)\|^2_{R_C} \right) \mathrm{d}t + \| \boldsymbol{x}(t_{\mathrm{s}}+T_{\mathrm{h}}) - \boldsymbol{x}_{\mathrm{ref}}(t_{\mathrm{s}}+T_{\mathrm{h}})\|^2_{P_C} \quad (13a)$$

$$\text{s.t. } \boldsymbol{F}(\dot{\boldsymbol{x}}(t),\boldsymbol{x}(t),\boldsymbol{u}(t),z(t),\boldsymbol{p}) = 0, \forall t \in [t_{\mathrm{s}}, t_{\mathrm{s}}+T_{\mathrm{h}}] \quad (13b)$$

$$\boldsymbol{h}(\dot{\boldsymbol{x}}(t),\boldsymbol{x}(t),\boldsymbol{u}(t),z(t),\boldsymbol{p}) \leq 0, \forall t \in [t_{\mathrm{s}}, t_{\mathrm{s}}+T_{\mathrm{h}}] \quad (13c)$$

$$\boldsymbol{x}(t_{\mathrm{s}}) = \hat{\boldsymbol{x}}(t_{\mathrm{s}}) \quad (13d)$$

$$\boldsymbol{x}(t_{\mathrm{s}}+T_{\mathrm{h}}) = \boldsymbol{x}_{\mathrm{ref}}(t_{\mathrm{s}}+T_{\mathrm{h}}). \quad (13e)$$

The objective is to minimize a cost function defined as the root mean square (RMS) error between the actual course and the reference, as given in Eq. (13a), in which Q_C, P_C, and R_C are weighting matrices. The objective associated constraints are the kite dynamics (Eq. 13b) and system bounds (Eq. 13c), similarly to Eq. (10). In addition, Eq. (13d) specifies the initial condition of the problem, setting it to the current state estimate $\hat{\boldsymbol{x}}(t_{\mathrm{s}})$. The terminal condition Eq. (13e) guarantees that the system comes back to the reference path by the end of the prediction horizon.

Within AWEbox, both the trajectory generation and path tracking OCPs are formulated as non-linear programs (NLPs) using the symbolic formalism from CasADi (Andersson et al., 2019). Then the interior-point NLP solver IPOPT (Wächter and Biegler, 2006) is used with the linear solver *MA57* (HSL, 2022). The discretization of the OCPs is achieved through direct collocation with Radau 4th-order polynomials. Additional implementation details are provided in De Schutter et al. (2023).

A two-way coupling is established between the flow solver, in which the aerodynamic forces and moments are computed, and the dynamics and control module. At each time step, the kite AL model evaluates the aerodynamic forces and moments, given the current state vector $\boldsymbol{x}^n$ and the flow data. Those forces and moments are then transmitted to the dynamics and control module. Within the latter module, the NMPC controller updates the control inputs vector $\boldsymbol{u}$ at regular time intervals, based on the deviation from the reference trajectory. The updated control inputs are then used to compute the next state $\boldsymbol{x}^{n+1}$, given the 6-DOF AWES dynamics. The integration of the dynamics is performed using a fourth-order Runge–Kutta scheme. The next state is then sent to the flow solver, and the process starts over. Again, for the NMPC, the simplified analytical aerodynamic model described in Sect. 2.5.1 is used.

The coupling algorithm of the LES and AL kite model with the dynamics and NMPC flight path tracking is depicted in Fig. 4. The flow solver, the dynamics, and the control have different characteristic time scales. During one flow time step $\Delta t_{\mathrm{fluid}}$, once the forces and moments are evaluated, the dynamics are integrated with a time step Δt_{dyn}. The control is evaluated only when the time is a multiple of NMPC sampling period T_c. Both processes run sequentially, each waiting for the other to send its data before proceeding. In general, $T_c > \Delta t_{\mathrm{fluid}} > \Delta t_{\mathrm{dyn}}$. The forces and control actions stay constant between two evaluations.

3 Accuracy verification

The wingspan of the kite drives the numerical discretization size of the problem. Here, the wingspan b is quite small compared to the trajectory that it flies, and hence many grid points are needed in the numerical flow domain. In a previous work (Crismer et al., 2024), the trajectory diameter D was about $5b$, and we used a domain with a frontal area of $3D \times 3D$. The wingspan corresponded to about 17 grid points (when the AL is aligned with the grid), and the total domain contained about 50 million cells. In this work, the trajectory diameter is taken twice larger, so as to better reproduce realistic trajectories. This section thus aims at defining the discretization and domain size requirements in order for the simulation to be as accurate as possible while maintaining an affordable computational cost, as is required to be able to investigate multiple scenarios.

3.1 Wing discretization

In this section, we investigate the requirements in terms of flow solver grid cell points and AL control points to ensure a good representation of the wing aerodynamic properties. To this end, the aircraft, without its control surfaces, is considered in steady level flight at an angle of attack of $-5°$. The aircraft has a zero-lift angle of $-11°$.

The chosen number of grid points per wingspan sets the flow solver grid cell size. The number of AL control points must be larger, yet it can be "only a bit larger" (i.e., about 1.2 times larger). This lower bound was determined such that the discretized AL takes full advantage of the grid resolution for the velocity sampling but without overkill (i.e., in the sense that using more control points does not improve the results further) – see Trigaux et al. (2024a). Concerning the mollification width σ of the Gaussian template, it is taken to be 2 h, where h is the flow solver grid size (Trigaux et al., 2024a).

Figure 5 shows the distribution of the lift and drag coefficients for different numbers of grid points per wingspan. We have $\sigma = \bar{c}/4$ for the highest resolution and $1.5\,\bar{c}$ for the lowest one. One can note that the accuracy is still very good close to the tip for the lowest resolution. The main differences ap-

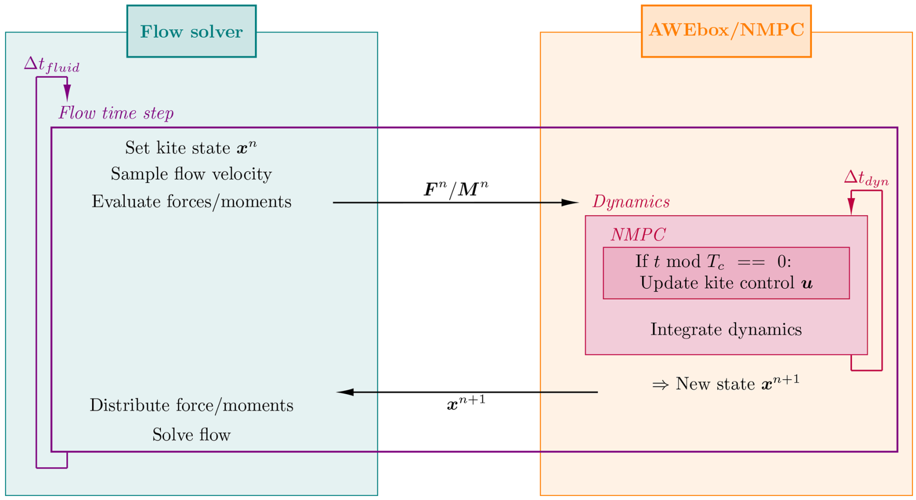

Figure 4. Schematic of the coupling of the flow solver and aircraft model with the dynamics and path tracking modules.

pear near the middle of the wing, where the lowest resolution leads to an overestimated lift and underestimated drag. The total lift coefficients are 0.604, 0.619, and 0.627 for 96, 32, and 16 points per wingspan, respectively. The total drag coefficients are 0.0237, 0.0234, and 0.0228, respectively. The difference between the finest and coarsest resolutions is $< 4\,\%$ for both lift and drag. This indicates that, despite the slight difference in loading in the middle of the wing, 16 grid points are enough to still have a fairly accurate representation of the wing aerodynamic loads. This also corresponds to the resolution used in Crismer et al. (2024).

When varying the number of AL control points for a given number of grid points per wingspan, here 16, the wing loading hardly changes at all, as depicted in Fig. 6. The difference in terms of total lift and drag is of the order of a 10th of a percent. The accuracy is therefore conserved regardless of the number of control points, as long as it is higher than the number of grid points. In the following, 1.2 times the number of grid points will be used.

3.2 Domain size

To investigate the domain size, the single-loop trajectory from Crismer et al. (2024) is flown with MPC path tracking in domains of different sizes. The trajectory diameter D is about $5b$. The domain is $9D$ long and has a square frontal area of height H, with periodic conditions on the sides, and slip conditions on the top and bottom (ground location). The trajectory was flown, in domains with $H = 2D$, $3D$, and $6D$. Assuming a circular trajectory orthogonal to the mean wind, the swept area of the trajectory corresponds to 15.7 %, 7.0 %, and 1.7 % of the total frontal area, respectively. The mean power measured during 12 power cycles after the flow is developed is 770.8, 777.7, and 775.3 kW, respectively. The greatest difference is less than 1 %, which indicates that a domain with $H = 2D$ is already enough for the flow to have negligible blockage effects. In this work, we consider larger trajectories for which the diameter is about $10b$. Since the ratio of the swept area to the frontal area scales with b/D, increasing D reduces the swept-area fraction for a given domain size, expressed in terms of D.

4 Simulation setup

This section details the different simulation parameter choices. We first detail the trajectory generation and control in Sect. 4.1. The computational settings of the LES are given in Sect. 4.2.

4.1 Trajectory and control

The trajectory is a four-loop trajectory, generated using `AWEbox`. It is computed for a uniform inflow $U_\infty = 12\,\mathrm{m\,s^{-1}}$. It is depicted in Fig. 7. The resulting trajectory has a spatial footprint of $674\,\mathrm{m} \times 494\,\mathrm{m} \times 407\,\mathrm{m}$. We define a characteristic length $D = 10b$, which approximately corresponds to the "characteristic diameter" of the trajectory (see Fig. 8). The kite rotates clockwise when looking downstream. The kite flight velocity ranges from 16.4 to $89.4\,\mathrm{m\,s^{-1}}$ over the whole trajectory, with an average value of $55.6\,\mathrm{m\,s^{-1}}$. The kite flies faster during the reel-out phase, with an average flight velocity of $67.8\,\mathrm{m\,s^{-1}}$, and reaches a minimum of $50.7\,\mathrm{m\,s^{-1}}$ at the end of the ascending parts of the loops. The velocity then decreases drastically during the reel-in phase. The trajectory has a time period $T_\mathrm{p} = 112\,\mathrm{s}$, and we define the dimensionless time t^* as t/T_p. A fraction of the fourth loop is used for starting the reel-in. The reel-out phase accounts for 70 % of the time and the reel-in phase for 30 %. The average power output is 1.38 MW, and the instantaneous power can turn negative in the ascending phase of each loop to help the kite reach the top of the loop.

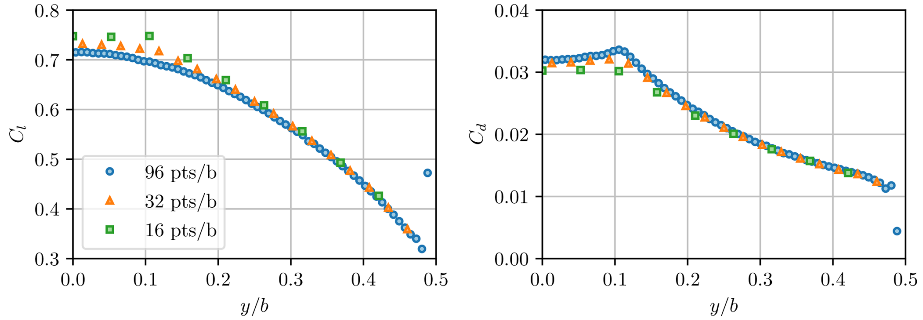

Figure 5. Comparison of the lift and drag coefficient distributions along the half span for different numbers of grid points per wingspan and with 1.2 times more AL control points.

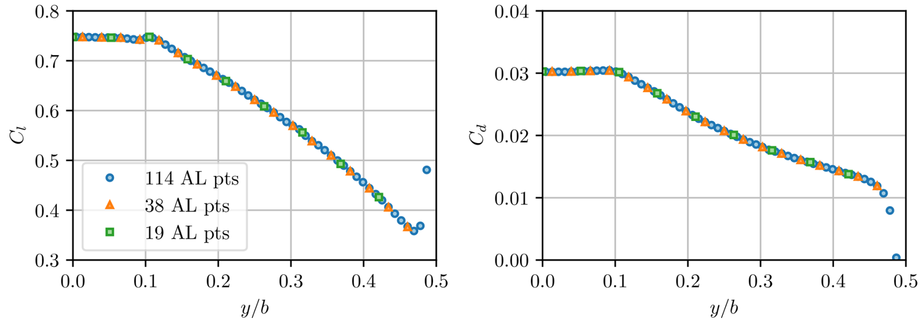

Figure 6. Comparison of the lift and drag coefficient distributions along the half span for different AL control points discretization, with 16 grid cell points per wingspan.

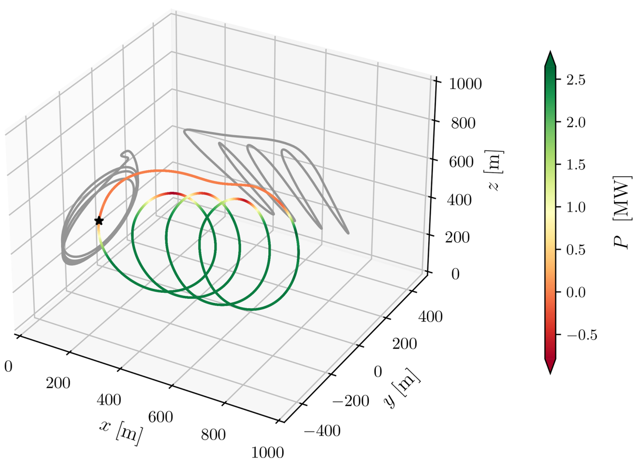

Figure 7. Four-loop trajectory generated using `AWEbox`, colored according to the instantaneous power output.

It should be noted that the trajectory is optimized for the given set of parameters and would therefore differ for other wind profiles. In the case of a uniform inflow, the kite flies at the lowest feasible altitude to limit the tether length and elevation angle. For a sheared inflow, the altitude-dependent wind velocity also plays a role, and the optimal trajectory may reach higher altitudes because of the lower wind speed near the ground. However, increasing the tether length and the elevation angle is detrimental to power production.

The set of constraints is applied to the state and control variables. They are provided in Appendix B, in Tables B1 and B2, along with the other constraints of the OCP and the NMPC. In addition to states and control variables, the instantaneous power is also constrained to limit the $P_{\mathrm{max}}/P_{\mathrm{avg}}$ ratio. There are also constraints on aerodynamic quantities, such as the angle of attack and the side-slip angle of the aircraft, and on the acceleration and tether force. The constraints are chosen to ensure operation within limits considered acceptable for the different components of the system. They are tightened during the trajectory generation to have some additional freedom and margin during the flight path tracking.

The kite controller is based on NMPC, as described in Sect. 2.5.2. The prediction horizon T_{h} of the NMPC corresponds to 20 NMPC sampling periods $T_c = 0.10$ s. During one sampling period, the dynamics are integrated 20 times, each dynamics time step being 0.005 s.

4.2 LES setup

The size of the domain is $5.4D \times 2.0D \times 1.36D$. This leads to a swept area corresponding to 11.5 % of the domain frontal area, which is shown to be sufficient in Sect. 3.2. The domain

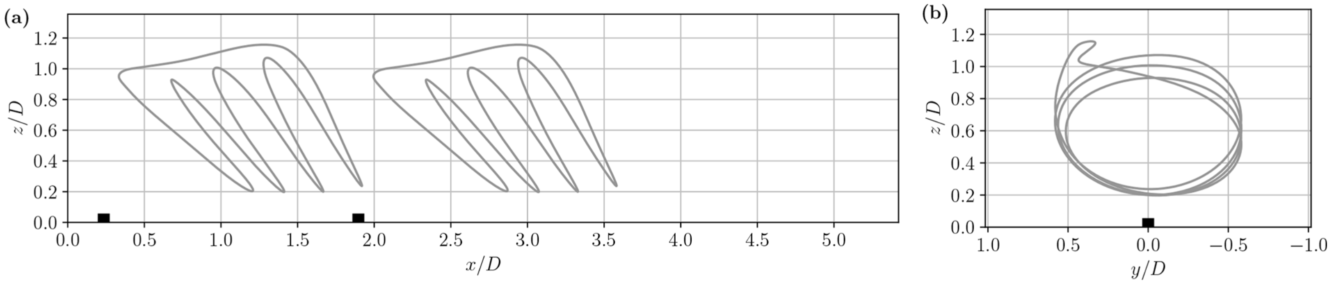

Figure 8. Illustration of the computational domain and flight region of the two kites, shown in side view **(a)** and front view **(b)**. Black rectangles indicate the tether attachment points, corresponding to the ground station locations.

is discretized using $1024 \times 384 \times 256$ grid cells, which corresponds to a uniform spatial resolution of 2.25 m. This leads to 19 grid cells per wingspan. We use periodic conditions on the sides, and slip conditions on the top and bottom. The domain is shown in Fig. 8. The lower boundary of the domain corresponds to the ground, and the z coordinate therefore denotes the altitude. The first kite trajectory is located so that it stays at least 3 wingspans away from the inlet. When there is also a second kite, it is placed as close as possible, ensuring that the tethers do not intercept (straight tethers). As the study focuses on the turbulent nature of the inflow and the kite's flight, we chose a uniform inflow of $12\,\mathrm{m\,s^{-1}}$, with a synthetic turbulence obtained using the Mann algorithm. The turbulence intensity is 6 % and is representative of offshore ABL conditions. The pre-computed box of turbulence has a spatial resolution of 4.5 m and is therefore linearly interpolated at the domain inlet. The box is long enough to last six power cycles. The time step used for the flow solver is 0.020 s. The investigations are carried out after the flow and the wake have developed during two power cycles (which corresponds to flowing 1.17 times the entire length of the domain) and during six additional power cycles.

5 Results and discussion

This section presents the results obtained for the various cases investigated. The first subsection is dedicated to the results obtained for a single kite. The next subsections detail the results for two kites, when the second one is placed behind the first one, and at different locations.

5.1 Single kite

When the kite flies alone, it is only subject to the inflow velocity wind and its turbulence. In the case of a uniform turbulent inflow with 6 % turbulence, the kite follows the trajectory without particular difficulty. The different quantities studied are represented as the average of what is performed by the kite during the six power cycles analyzed. A shaded area surrounds that average, and it corresponds to plus and minus 1 standard deviation. In the different plots, the time is made dimensionless using T_p, the reference trajectory period, which is 112 s. Figure 9 shows the results for position and attitude (Euler angles). One can see that those are very close to the reference and that the inter-cycle variation is almost nil. The RMS error in position is at most $1.1b$. As previously noted, the flight altitude in a uniform inflow is low and reaches the specified lower bound.

The actuation of the control surfaces is presented in Fig. 10. Although it remains close to the references, some deviations result from the controller mitigating the turbulence of the inflow. The average deflection of the ailerons remains fairly close to the reference, while it varies significantly from one cycle to another. The elevator actuation shows fast variations, yet up to a maximum of 6°, and the rudder is a bit less used at maximal positive deflection than planned. The reel-in phase, where the kite will roll and pitch to come back facing the wind, is well identifiable after $t/T_\mathrm{p} = 0.7$.

The force and moment coefficients in the body frame are provided in Fig. 11. The forces from the simulations are close to those from the reference. The vertical force coefficient C_z remains quite constant during the reel-out phase. Regarding the moments, the rolling and pitching moments are quite noisy. This likely indicates a larger mismatch between the simplified model and the AL-based model for these quantities. The yawing moment is more precisely reproduced. The moments show a high variability due to the encountered perturbations and the actuation of the control surfaces used to mitigate them.

The tether acceleration and traction, and the power output are very well followed, as seen in Fig. 12. The averaged cycles are close to the reference, and the inter-cycle variation is very low. One can see that the tether speed turns negative at the end of each loop. This is what makes the power negative and helps the kite to go up at the end of the ascending phase of a loop, as pointed out in Sect. 4.1. The reel-in phase can be identified as the tether speed becomes highly negative at the end of the power cycle. The tether traction is always positive, and it reaches maxima when the kite is at the bottom of the loop with maximum velocity. It is interesting to note that the tether traction is here null during the reel-in phase, corresponding to zero power consumption. The fact that it

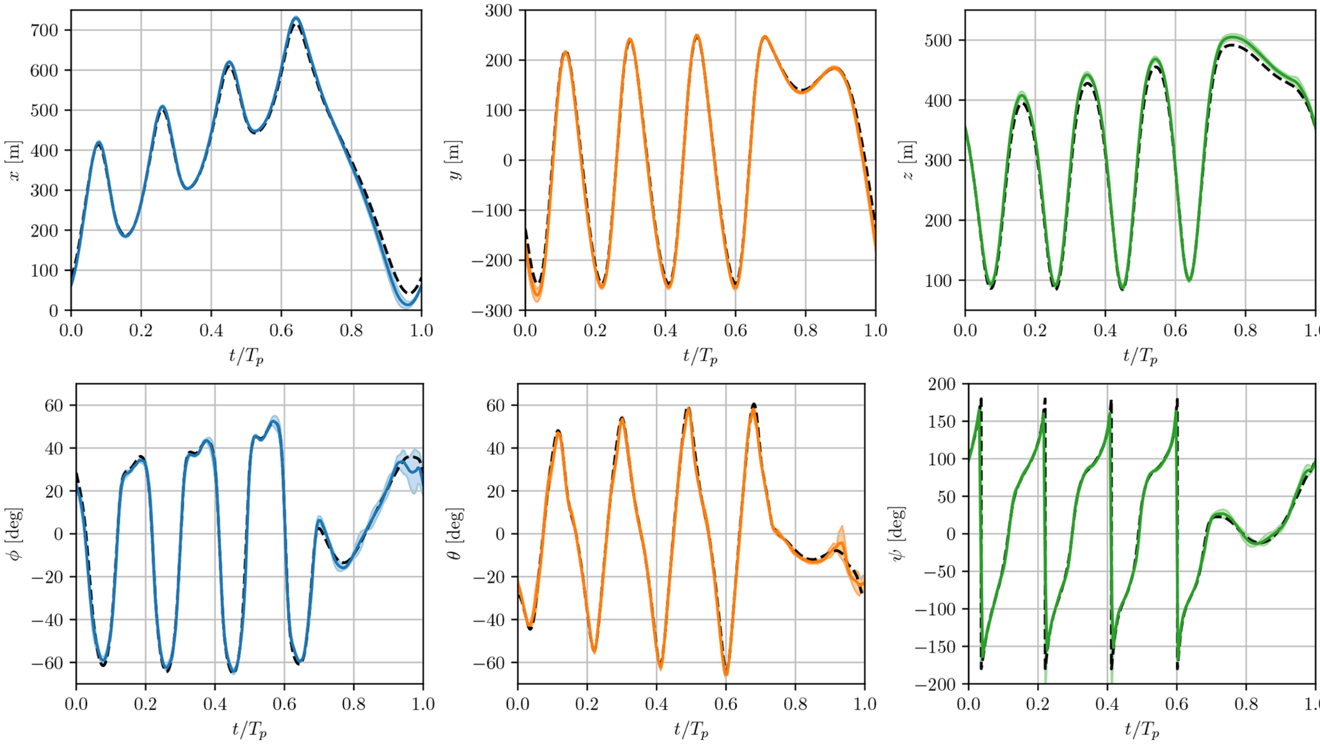

Figure 9. Six-cycle averages of the position and Euler angles, shown as solid colored lines, with the corresponding standard deviation indicated by shaded areas, for LES with an AL model in a 6 % turbulence intensity (TI) flow. The `AWEbox` reference is indicated by the dashed black line.

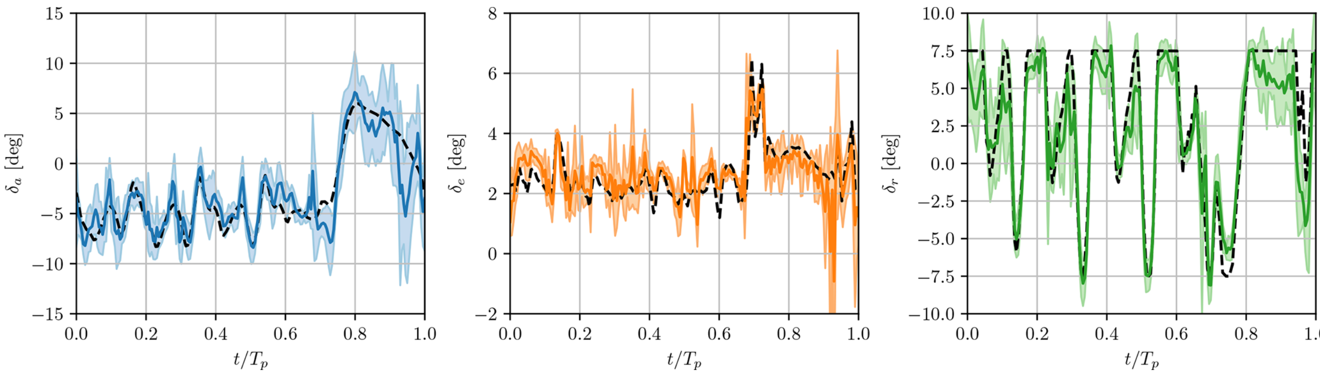

Figure 10. Six-cycle averages of the control surfaces deflection angle, shown as solid colored lines, with the corresponding standard deviation indicated by shaded areas for LES with an AL model in a 6 % TI flow. The `AWEbox` reference is indicated by the dashed black line.

is zero is due to the simplified hypotheses of the `AWEbox` model (there is no model for the generator and the drum, and the tether is considered straight). During the reel-in phase, the kite essentially flies like a glider. It compensates for both its weight and that of the tether and is continuously descending – all of that without energy consumption. Here, the kite only consumes energy at the end of each loop, during the ascending phase.

One can also note that the tether traction, which is closely related to the vertical force on the kite, fluctuates a lot during the power cycle. During the reel-out phase, its standard deviation is 43 % of the mean value. In contrast, the vertical force coefficient is more or less constant during the reel-out, with a standard deviation of only 5 % of its mean value during reel-out. The kite flight speed experiences large fluctuations, and so does the relative air velocity, resulting in large variations in vertical force magnitude. The averaged power is also close to the reference, despite some deviation during the first and fourth loops. The inter-cycle variation is quite low. The power production reaches a plateau during each loop due to the maximal power constraint. The total average power production is 1.39 MW, to be compared to the 1.38 MW planned

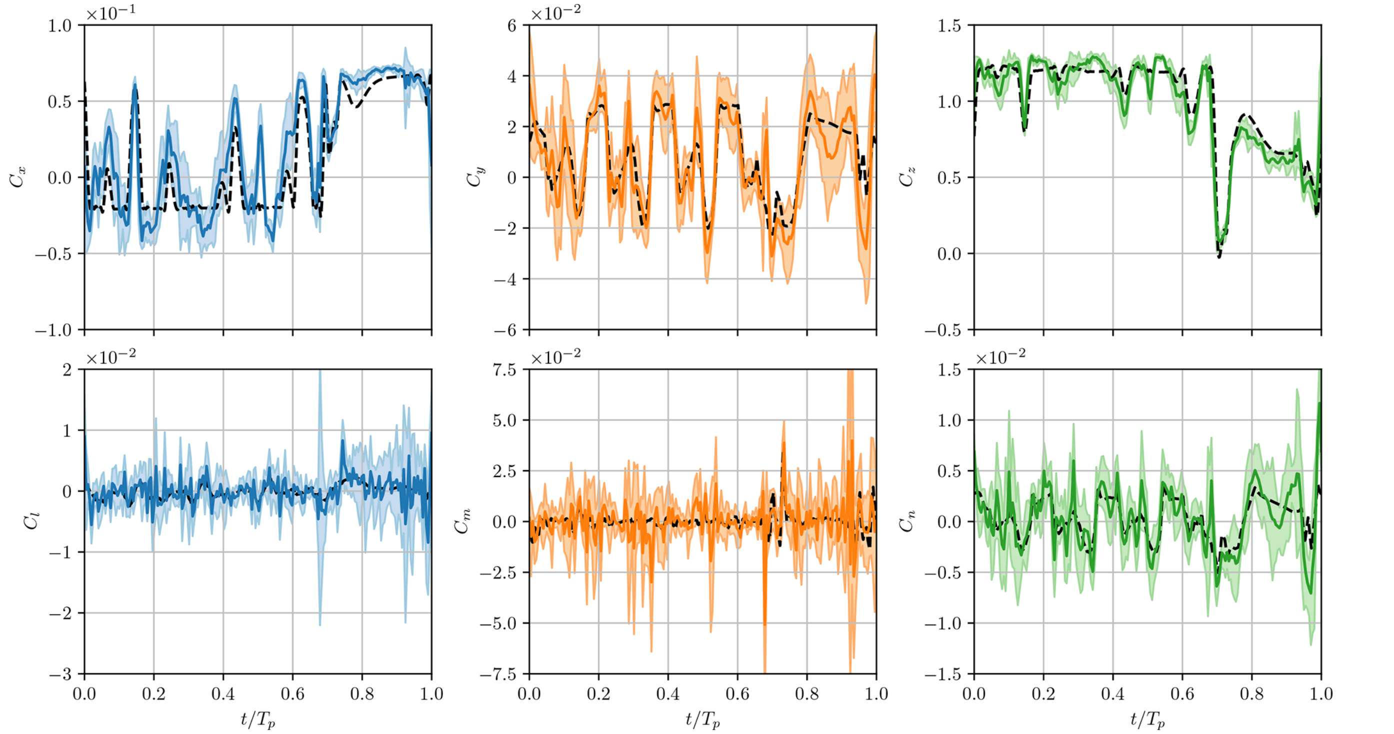

Figure 11. Six-cycle averages of the forces and moments expressed in the body frame, shown as solid colored lines, with the corresponding standard deviation indicated by shaded areas for LES with an AL model in a 6 % TI flow. The `AWEbox` reference is indicated by the dashed black line.

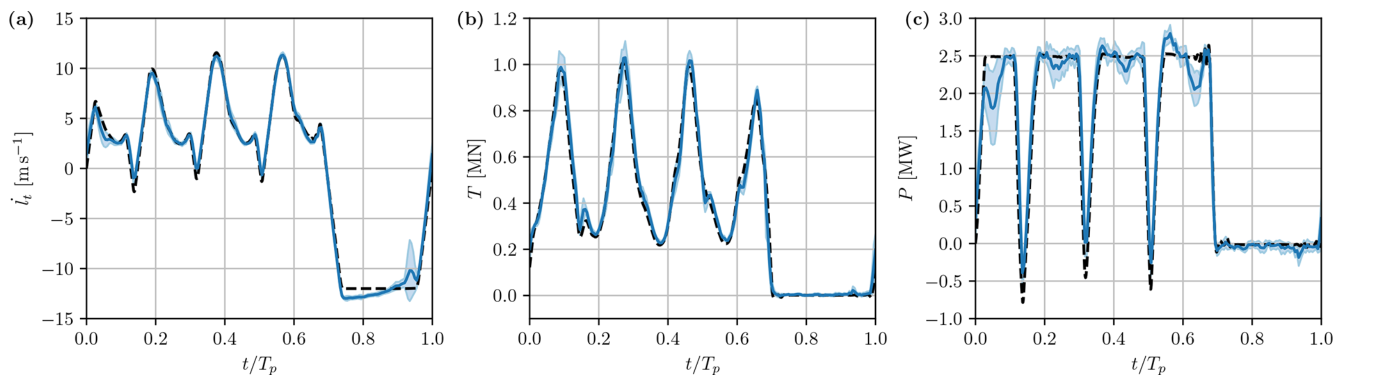

Figure 12. Six-cycle averages of the tether speed **(a)**, tether traction **(b)**, and power **(c)**, shown as solid colored lines, with the corresponding standard deviation indicated by shaded areas for LES with an AL model in a 6 % TI flow. The `AWEbox` reference is indicated by the dashed black line.

by `AWEbox`. The RMS error on the mean power output of the six flown power cycles is 0.8 % of the reference power output.

The angle of attack and wing loading along the span are displayed in Fig. 13, where $\boldsymbol{f}_{\mathrm{a}}$ stands for the aerodynamic force per unit length. Let us first note that the loading is almost symmetric during the reel-in phase because the kite comes back in a quasi-level flight toward its anchor point and with a reduced loading. However, it is slightly skewed toward the starboard side of the wing during the reel-out phase due to the rotation. In terms of force coefficient, the average loading barely varies during the reel-out phase, as does the angle of attack. However, as already pointed out, it varies greatly in terms of magnitude due to the large variation of the flight velocity. The effect of the ailerons ($0.31 \leq \| y/b \| \leq 0.47$) is well marked. The port (left) aileron is deflected down, increasing lift; and the starboard (right) aileron is deflected up, decreasing lift. This counteracts the asymmetric loading induced by the rotation, i.e., induced roll, which would otherwise make it roll toward the interior of the loop.

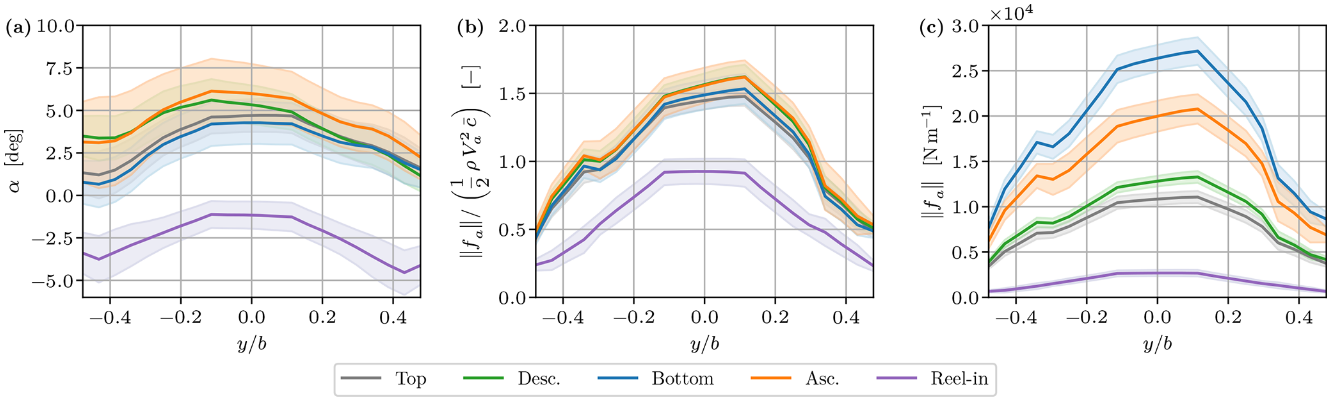

Figure 13. Six-cycle averaged aircraft angle of attack **(a)** and wing loading, dimensionless **(b)** and dimensional **(c)**, together with their standard deviation (shaded area) for LES with AL in a 6 % TI flow. They are represented when the kite is at the top and bottom positions, and in the middle of the descending and ascending phases of the reel-out loops, as well as during the reel-in phase.

A vertical longitudinal cut of the mean streamwise velocity field is displayed in Fig. 14. Three key features can be identified. First, the velocity deficit is predominantly located in the lower part of the trajectory. This behavior has also been reported by Haas et al. (2019) and Crismer et al. (2023), who also observed that the lower portion of the wake spreads more rapidly in the radial direction. In the present case, the weaker velocity deficit in the upper part of the wake can be partly attributed to the fact that the kite reaches different altitudes in the upper parts of the loops, whereas the lower parts reach the lower altitude bound and therefore occur at nearly the same altitude. However, this lower velocity deficit on the upper part is also reported for purely circular single-loop trajectories in Crismer et al. (2023). Second, the wake is deflected downward. This deflection results from the tilted rotation plane and the presence of a vertical component in the aerodynamic force acting on the kite. A similar effect is observed for tilted wind turbines (Trigaux et al., 2020). Finally, the magnitude of the normalized velocity deficit is fairly low and goes only up to $0.06\,U_\infty$. For comparison, the velocity deficit of wind turbines can be on the order of $0.3\,U_\infty$, even a few diameters downstream of the turbine; see for instance (Coquelet et al., 2022).

Figure 16 shows the velocity deficit in cross-flow planes. The averaged force density, computed from the forces predicted by `AWEbox` and derived from the analogy with an actuator annulus, is plotted in Fig. 16a. The first step in establishing this analogy is to obtain a force distribution along the kite trajectory that is constant in time, such that the integral of this force distribution equals the time-averaged streamwise (axial) force:

$$\frac{1}{T_\mathrm{p}}\int_0^{T_\mathrm{p}} F_x(t)\,\mathrm{d}t = \int_0^{L} f_x(s)\,\mathrm{d}s, \tag{14}$$

where F_x denotes the instantaneous total axial force acting on the kite, f_x is the axial force distribution per unit length along the trajectory, and s is the curvilinear coordinate along the trajectory. The trajectory has a total length L and a time period T_p. The force distribution $f_x(s)$ can be expressed by introducing the change of variable $s = s(t)$, so that $\mathrm{d}s = \|\dot{\boldsymbol{q}}(t)\|\,\mathrm{d}t$, and by imposing equality of the integrands:

$$\frac{1}{T_\mathrm{p}}\int_0^{T_\mathrm{p}} F_x(t)\,\mathrm{d}t = \int_0^{T_\mathrm{p}} f_x(s(t))\,\|\dot{\boldsymbol{q}}(t)\|\,\mathrm{d}t$$
$$\Rightarrow f_x(s(t)) = \frac{F_x(t)}{\|\dot{\boldsymbol{q}}(t)\|\,T_\mathrm{p}}. \tag{15}$$

The force per unit trajectory length f_x (in $\mathrm{N\,m^{-1}}$) is then distributed across the span to obtain a surface force density f_x/b (in $\mathrm{N\,m^{-2}}$). This force density is projected onto a single plane to obtain the equivalent actuator annulus. Figure 16a shows that the aerodynamic forces are mainly concentrated in the lower-left part of the trajectory, between the lowest point and the first half of the ascending phase. This is also what is observed in Fig. 15, which shows the norm of the total aerodynamic force $\boldsymbol{F}_\mathrm{a}$ along the trajectory.

A prediction of the time-averaged wake velocity can then be obtained from the momentum conservation. In a reference frame moving at the reel-out velocity $U_{r,x}$ (here taken as the streamwise projection of the tether speed), the momentum conservation yields

$$f_x = \rho \int_{-\xi}^{\xi} \bar{U}\left((U_\infty - U_{r,x}) - \bar{U}\right)\mathrm{d}r, \tag{16}$$

where the integration bounds $\pm\xi$ delimit a control volume across the annulus, and $\bar{U} = \bar{U}(r)$ is the wake velocity profile at its downstream boundary, where it is assumed that the

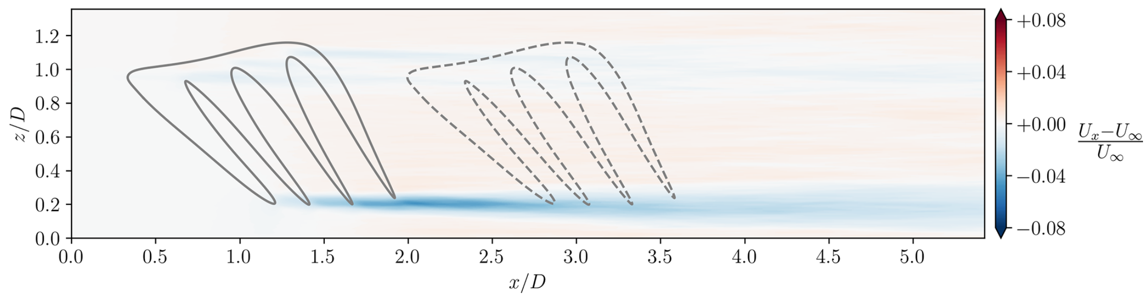

Figure 14. Six-cycle averaged streamwise velocity deficit of a single-kite wake in a vertical longitudinal plane at the center of the trajectory. The location of a virtual kite downstream is indicated by a dashed line.

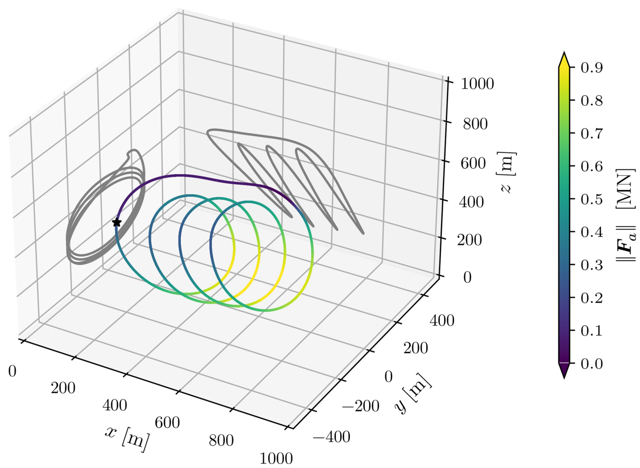

Figure 15. Four-loop trajectory generated using AWEbox, colored according to the norm of the aerodynamic force.

pressure has recovered to p_∞. Further adopting the simplified Betz approach (i.e., assuming that Bernoulli's equation applies between the force application point and the wake plane) and using a top-hat profile of width b_w for the wake velocity deficit leads to

$$f_x \simeq \rho\, U_\mathrm{w}^* \left((U_\infty - U_{r,x}) - U_\mathrm{w}^*\right) b_\mathrm{w}, \tag{17}$$

where $U_\mathrm{w}^* = U_\mathrm{w} - U_{r,x}$ is the wake velocity in the moving frame. Using the mass conservation gives $b\,(U_\infty + U_\mathrm{w}^*)/2 = b_\mathrm{w}\, U_\mathrm{w}^*$ and taking the wake velocity back in the fixed reference frame, one obtains the following estimation:

$$\frac{f_x}{b} \simeq \frac{1}{2}\rho \left((U_\infty - U_{r,x})^2 - (U_\mathrm{w} - U_{r,x})^2\right)$$
$$\Leftrightarrow U_\mathrm{w} = \sqrt{(U_\infty - U_{r,x})^2 - \frac{f_x}{b}\frac{2}{\rho}} + U_{r,x}. \tag{18}$$

This equation is only valid if the term inside the square root is positive. This justifies the use of the streamwise projection of the tether speed as the approximate reel-out velocity instead of the local streamwise velocity of the kite. This velocity deficit estimation is shown in Fig. 16b. The axial force representation already provides insight into the wake shape. The velocity deficit is concentrated in the lower half of the loop and is slightly rotated clockwise, corresponding to the regions where the aerodynamic forces are largest. Overall, the estimated velocity deficit slightly overpredicts the measured wake deficit. This discrepancy is due to the simplifying assumptions introduced above. In particular, all forces were collapsed onto a single plane, whereas the trajectory spans a wide range in x, and the high ambient turbulence rapidly mixes the wake. However, the distribution of the deficit is well predicted, as depicted in Fig. 16c–f, and a follower kite will therefore experience a lower wind speed when flying in that area.

The deficit decreases in intensity as it is advected downstream, while its shape remains essentially unchanged. The low averaged velocity deficit is due to the nature of the wake produced by such four-loops trajectory. Indeed, the loading of the kite is very low during the reel-in phase, which accounts for 30 % of the trajectory time period, and the kite mainly produces a wake during the reel-out phase. The wake is therefore discontinuous in space and time, and released in batches, resulting in a low time-average velocity deficit.

Those discontinuities can be observed in Fig. 17, which shows an instantaneous streamwise-velocity deficit. On the

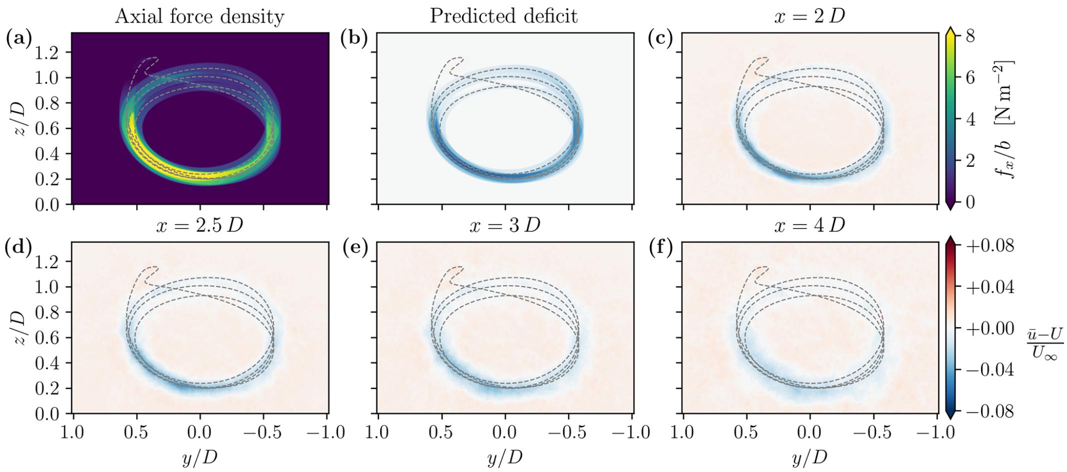

Figure 16. Six-cycle averaged streamwise velocity deficit of a single-kite wake in transversal planes at different positions downstream of the kite **(c–f)**. The projection of the x-force density along the trajectory is represented in the upper-left panel **(a)**, along with the resulting velocity deficit prediction **(b)**. The trajectory is indicated by a dashed line.

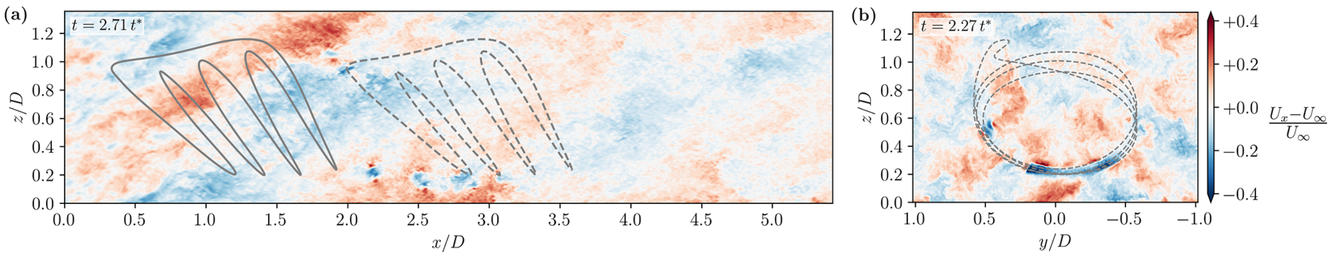

Figure 17. Instantaneous streamwise velocity deficit of a single-kite wake in a vertical longitudinal **(a)** and transversal plane at $1.6D$ from the inlet **(b)**.

left, a longitudinal (a) cut shows the instantaneous velocity deficit just after the kite lowest position in its fourth loop. The passage of the kite left traces around $z \simeq 0.2D$ at $x \simeq 2.2$, 2.5, 2.8, and $3.1D$. Those traces have already decreased in intensity since the time they were released and are no longer stronger than the ambient turbulence. The maximum deviation from the inflow velocity in that cut is 33 %, and it will become even lower by the time it reaches the flight area of the second kite. However, in the vicinity of the kite, the induced velocity can be quite significant. The transversal cut is taken when the kite is near its maximal loading, at the bottom part of the second loop. The position and near wake of the kite is clearly identifiable, and the velocity deficit in that plane goes as low as 85 % of U_∞ (out of the color map range). It corresponds to the maximal velocity induced by the tip vortices. This observation is consistent with the kite's flight velocity at this stage of its trajectory, which reaches 89.4 m s^{-1}. Relative to its flight velocity, the deficit is only of 11 %. This is of the order of magnitude of the downwash that can be expected for such aircraft when flying at a high angle of attack.

5.2 Two kites in tandem

For the cases with two kites, both kites try to fly the same optimal reference trajectory. Two scenarios are investigated. For the first case, the second kite flies in-phase with the first kite. In the second case, the second kite trajectory is phase-shifted relative to the first kite's trajectory. In order to isolate the effect of the wake of the first kite, we perform additional simulations of the second kite only. Those simulations, hereafter referred to as "2nd only", will assess the effect of the ambient turbulence on kite 2.

5.2.1 In-phase flight

When the kites fly in-phase, the kites have, at every moment, the same reference state. In this specific scenario, the simulation shows that the second kite does not interact with the first kite's wake. This depends on the kite spacing, inflow velocity, and trajectory period.

Here, as illustrated in Fig. 18, the second kite reel-out occurs in almost unperturbed flow, and it reels in while the first kite wake is passing by. Furthermore, as the kite reels in on

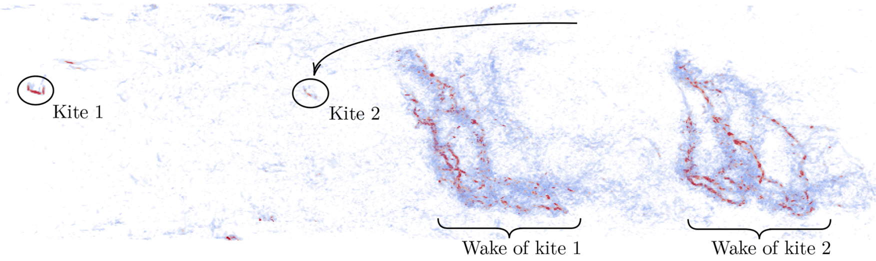

Figure 18. Instantaneous vorticity field volume rendering, at the beginning of a reel-out phase, for a two-kite configuration where the kites fly in-phase; illustrating the second kite avoiding the first kite's wake.

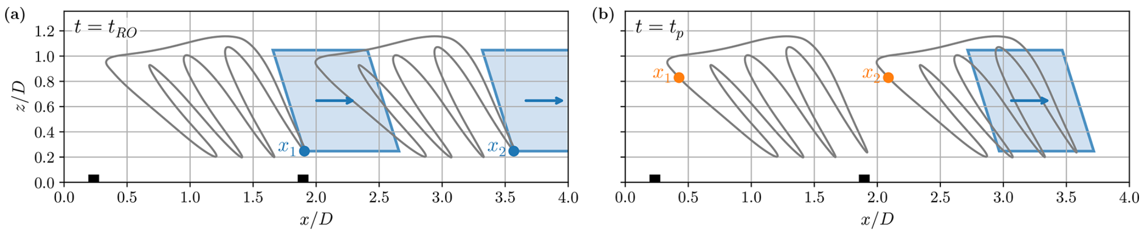

Figure 19. Schematic illustrating the wake interaction for a two-kite configuration with in-phase trajectories.

the side, it also avoids the wake. Therefore, the first kite wake does not affect the second kite's power production phase.

This can be verified through simple calculations. The reasoning is depicted in Fig. 19. In that figure, the parallelograms represent the wake of kites. The wake of the first kite is a structure released during its reel-out phase. At the end of this phase, at a time $t_{\mathrm{RO}} = n\,T_{\mathrm{p}} + T_{\mathrm{RO}}$, the wake of the first kite extends downstream, starting from the position of the first kite, $x_1(t_{\mathrm{RO}})$. At this time, both kites enter the reel-in phase, and the second kite reels in from $x_2(t_{\mathrm{RO}})$ to $x_2(t_{\mathrm{p}}) \simeq (806+70)\,\mathrm{m} = 876\,\mathrm{m} = 2.06D$. The start of the trajectory, at a time $t_{\mathrm{p}} = (n+1)\,T_{\mathrm{p}}$, corresponds approximately to the end of the reel-in phase. During this time interval, the wake of the first kite is advected downstream. The relevant question is therefore: where is the wake of the first kite when the second kite starts its reel-out phase? The wake of the first kite is advected from $x_1(t_{\mathrm{RO}})$ over a duration of $T_{\mathrm{p}} - T_{\mathrm{RO}} \simeq 41\,\mathrm{s}$ at an advection velocity of U_{adv}. Here, the advection velocity within the wake is assumed to be slightly lower than the mean inflow velocity and is estimated to be approximately $11\,\mathrm{m\,s^{-1}}$ (see Fig. 14). At $t = t_p$, the wake is therefore located at $x_1(t_{\mathrm{RO}}) + U_{\mathrm{adv}}(T_{\mathrm{p}} - T_{\mathrm{RO}}) \simeq \big((100+715)+11\times 41\big)\,\mathrm{m} = 1266\,\mathrm{m} = 2.99D$. When the second kite resumes its trajectory, the wake of the first kite is already far downstream.

The second kite experiences almost no additional perturbation other than ambient turbulence and operates as efficiently as the first kite. The mean power is 1.39 MW for the first kite and 1.40 MW for the second kite. Figure 20 shows the error with respect to the reference. It is evaluated by taking the RMS of the vector norm of the difference between the results and the reference, i.e., $\epsilon(\boldsymbol{q}) = \mathrm{RMS}(\|\boldsymbol{q} - \boldsymbol{q}_{\mathrm{ref}}\|)$ and $\epsilon(\boldsymbol{F}_{\mathrm{a}}) = \mathrm{RMS}(\|\boldsymbol{F}_{\mathrm{a}} - \boldsymbol{F}_{\mathrm{a,\,ref}}\|)$. In terms of position, the RMS error compared to the reference is limited to $1.1b$. For the forces, it goes up to 20 % of the force range but is most of the time below 10 %. It is also very close to the case without the first kite, confirming that the first kite has almost no influence on the operation.

The first and second kites' average power production cycles are very similar, as depicted in Fig. 21. Their mean power is 1.39 and 1.40 MW, respectively. The power output of the second kite is identical when the first kite is removed.

The average velocity deficit shown in Fig. 14 could suggest that the second kite has been exposed to lower velocities. However, as the four-loop trajectory is not continuous in its wake shedding, considering averaged flow quantities is not consistent for drawing conclusions about follower performance, as the second kite can avoid the wake. The averaged velocity deficit of the kite tandem is shown in Fig. 26a and b. The deficit is further increased by the second kite, from $0.05\,U_\infty$ to $0.08\,U_\infty$, and is enlarged.

5.2.2 Phase-shifted flight

In this case, the second kite trajectory is phase-shifted so that the second kite flies in the wake of the first kite during its reel-out phase, as shown in Fig. 22.

The trajectory of the second kite starts at $0.43\,t^*$, instead of 0. This phase shift is evaluated as follows. The second kite must start its trajectory once the wake of the first kite has advected over the distance separating the two-kite trajectories, equal to the distance between the ground stations L_s. This is illustrated in Fig. 23. The required delay is $T_{\mathrm{s}} = \frac{L_s}{U_{\mathrm{adv}}} = 64.2\,\mathrm{s}$. The second kite will start its trajectory

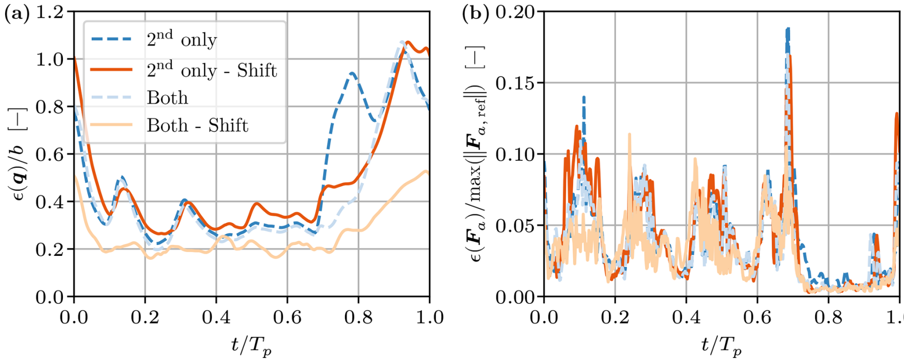

Figure 20. Six-cycle averaged position error $\epsilon(\boldsymbol{q}) = \mathrm{RMS}(\|\boldsymbol{q} - \boldsymbol{q}_{\mathrm{ref}}\|)$ **(a)** and aerodynamic force error $\epsilon(\boldsymbol{F}_{\mathrm{a}}) = \mathrm{RMS}(\|\boldsymbol{F}_{\mathrm{a}} - \boldsymbol{F}_{\mathrm{a,\,ref}}\|)$ **(b)** for the second kite flying in an LES with an actuator line (AL) representation in a flow with 6 % TI. Results are shown for both the in-phase and phase-shifted trajectories when flying in the wake of the first kite ("Both"). They are compared with a single-kite configuration at the same location and with the same time delay, i.e., with the first kite removed ("2nd only").

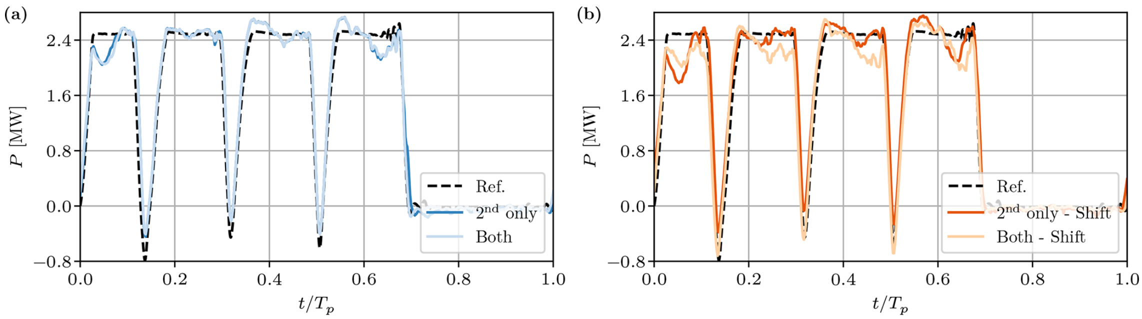

Figure 21. Six-cycle averaged power of the second kite flying in LES with AL in a 6 % TI flying the in-phase **(a)** or phase-shifted **(b)** trajectory; also compared to a "single" kite.

at $t_{\mathrm{s}} = n\,T_{\mathrm{p}} + T_{\mathrm{s}}$. Accordingly, the second kite starts the simulation at $T_{\mathrm{p}} - T_{\mathrm{s}} = 47.8$ s, corresponding to $0.43\,t^*$.

Again, the first kite experiences the same conditions than when it is alone and in the "in-phase" scenario. The second kite also flies well, and its tracking ability is only weakly affected, despite the perturbations it encounters, as evidenced by the "Shift" curves in Fig. 20. In Fig. 20a, the tracking error of the flown path with respect to the reference remains very small and does not exceed the error observed in the other cases. Indeed, the kite flies quite fast, and perturbations must be large enough compared to its velocity to become significant. For example, the turbulence intensity is evaluated with respect to U_∞, which is six times smaller than the mean kite speed during its reel-out phase. Turbulence levels expressed this way are therefore much less significant for the kite, which may explain why the kites are only weakly perturbed.

Similarly, the error on the force, shown in Fig. 20b, is of the same order of magnitude as in the other cases. As evidenced in Fig. 24, the aerodynamic force on the second kite is globally lower when it is in the wake of the first one. However, characteristic features are hardly identifiable. The evolution of the standard deviation of the aerodynamic force is also shown for both cases, and again no significant increase is observed. The RMS difference in terms of forces, evaluated on instantaneous data, goes up to 29 % of $\max(\|\boldsymbol{F}_{\mathrm{a}}\|) = 1.06$ MN, while it is only 3 % on average.

What the second kite effectively perceives is a modified inflow velocity. The flow velocity it experiences is obtained from a simulation in which the force distribution in the flow is switched off, and the second kite is used as a sensor. This prevents the measurement from being perturbed by the bound vortex and wake of the AL. The results are shown in Fig. 25 for the second kite flying alone and when in the wake of the first kite. Figure 25a shows that, overall, the sampled velocity is slightly lower throughout the reel-out phase. The standard deviation of the measured flow velocity, as provided in Fig. 25b, also increases slightly. Figure 25c shows that the difference in sampled velocity is largest when the aerodynamic force is highest, around $t/T_{\mathrm{p}} \simeq 0.1$, 0.28, and 0.45, which corresponds to the portions of the trajectory where the kite is on the bottom of the loops. This is also where the velocity deficit in the first kite's wake is primarily located. The difference in sampled velocity ranges from 0 % and 12 % of the inflow velocity. Similarly, the increase in standard deviation occurs mainly when the kite is at the bottom of the loops

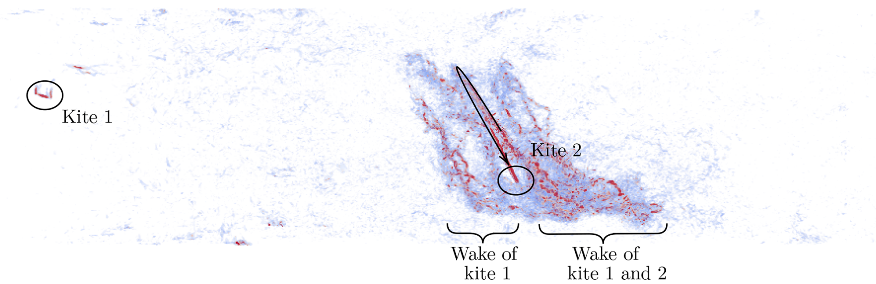

Figure 22. Instantaneous vorticity field volume rendering at the beginning of a reel-out phase of the first kite for a two-kite configuration where the kites fly out of phase, illustrating the second kite flying in the first kite's wake.

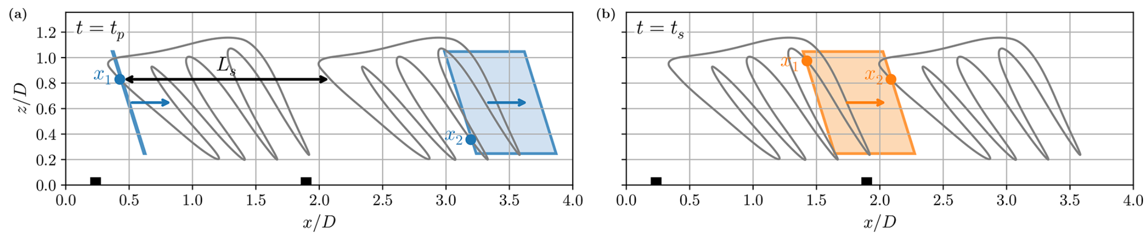

Figure 23. Schematic illustrating the wake interaction for a two-kite configuration with phase-shifted trajectories.

during the reel-out phase, and ranges from 0 % to 8 % of the inflow velocity. The RMS difference in terms of sampled velocity, evaluated on instantaneous data, goes up to 26 % of the inflow velocity while it is only 3.6 % on average. Again, this difference in sampled velocity is made dimensionless using the inflow velocity and is thus even smaller when compared to the kite flight velocity.

The velocity deficit induced by the wake of the first kite nevertheless affects the power production of the second kite. It can be observed in Fig. 21 that the power output is lower during fractions of the loops. It should be noted that it only happens at specific times. During the reel-out phase, the kites move downstream at a lower velocity than the inflow. As a result, the length of the wake packet is shorter than the streamwise extent of the reel-out portion of the trajectory. Consequently, the wake of the first kite can only affect the follower during a fraction of its reel-out phase. In this case, the kites produce 1.38 and 1.30 MW, respectively. The second kite thus produces roughly 6 % less than the first one.

The trajectory shift of the second kite also affects the wake. This is evidenced in Fig. 26c and d, which displays the difference in velocity ΔU between the phase-shifted and the in-phase cases. It shows that the velocity deficit for the phase-shifted case is weaker in the upper parts of the loops, around $z/D = 1$ in Fig. 26c. However, the deficit is further increased in the lower parts of the loops and broadened at around $z/D = 0.2$.

6 Conclusions

This paper presents a large-eddy simulation framework to perform simulations of ground-gen rigid-wing airborne wind energy systems. The framework is based on an LES flow solver developed in-house. Kites are represented by a model based on an actuator line for the main wing, complemented by models for the control surfaces (elevator, rudders, ailerons). In this framework, kites fly optimal trajectories as computed using `AWEbox` by solving optimal control problems. The flow solver is also coupled to the flight path tracking module of `AWEbox` to handle the control of the different kites in the simulation environment, using model predictive control.

The framework is employed to investigate both a single kite operating in a turbulent flow and a pair of kites, with the second one flying behind the first one. In the single-kite case, we highlight the capability of the kite to fly its trajectory despite the 6 % turbulence intensity. The MPC controller performs well in handling the encountered turbulence and perturbations. The different control states are followed accurately during flight path tracking. The position and attitude remain very close to the reference, while some variability is observed in the actuation of the control surfaces and in the forces and moments. The yawing moment is well reproduced, while the rolling and pitching moments experience more variations. The precision of the simplified aerodynamic model could likely be improved for those aspects. The wing loading is shown to vary quite significantly during the trajectory and is also skewed because of the rotation, but its shape does not vary much. The average velocity deficit from the

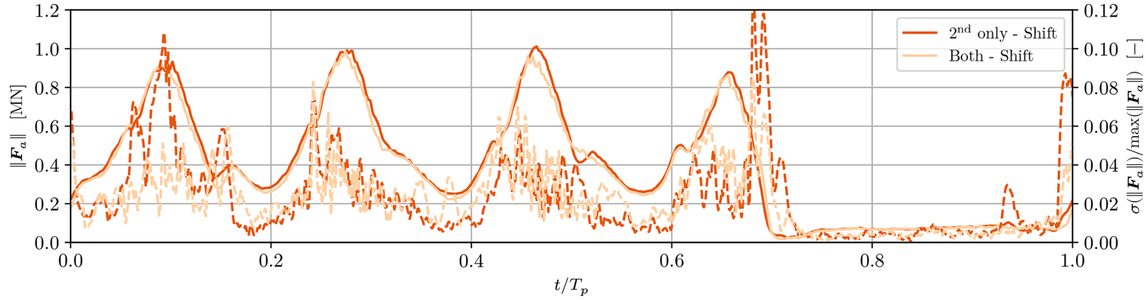

Figure 24. Six-cycle averaged aerodynamic force magnitude (solid line) and standard deviation (dashed line) for the second kite flying with or without the first kite in front in LES with AL in a 6 % TI flow.

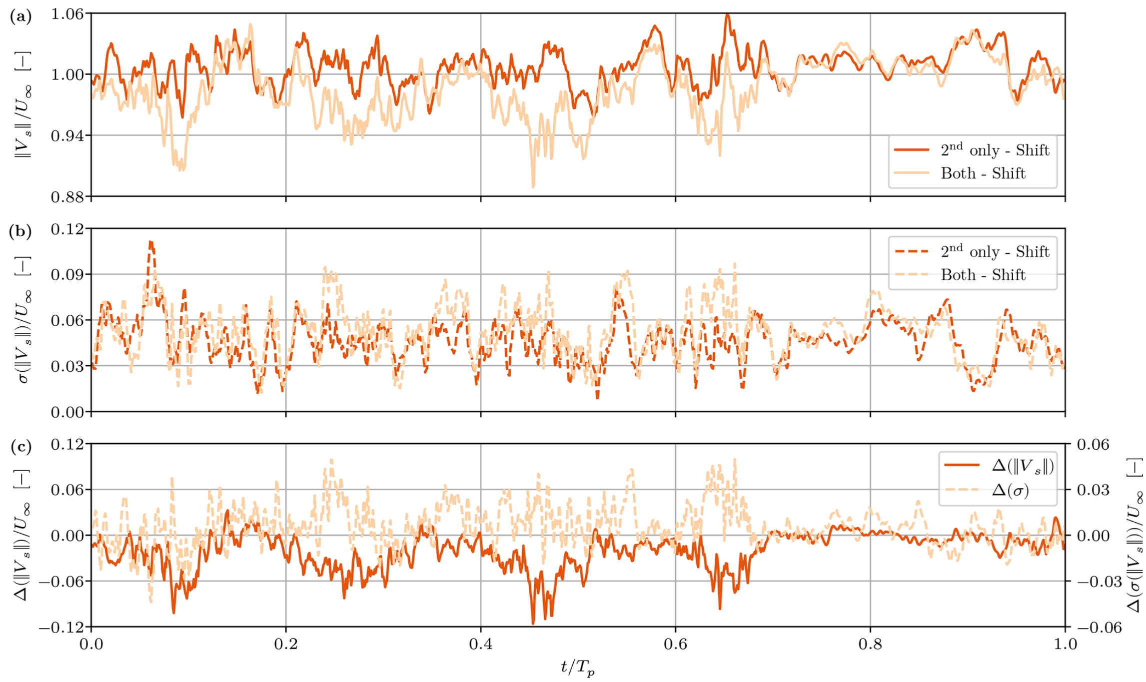

Figure 25. Six-cycle averaged mean sampled velocity on the wing **(a)** and its standard deviation **(b)** for the second kite flying with or without the first kite in front in LES with AL in a 6 % TI flow. The second kite is used here as a sensor and does not induce forces in the flow, so that the measurements are not perturbed by the wing bound vortex and wake. The differences between the cases with and without the first kite is also displayed **(c)**.

kite wake is weak. However, such trajectories produce discontinuous wakes in both space and time, so that the wake mostly induces local perturbations, which are not well characterized by the time-averaged velocity deficit.

In the first configuration of kites in tandem considered, the second kite is not perturbed at all by the wake of the first kite. It is a configuration where it reels in while the first kite wake passes by, and it completely avoids it. The tracking is therefore also accurate. In a second scenario, the second kite is forced to fly in the wake of the first kite, which is done by introducing a phase shift at the start of its trajectory. Concerning trajectory tracking, the encountered wake perturbations do not significantly affect the tracking ability of the second kite, and it correctly follows its trajectory. Nevertheless, there is a non-negligible impact on the power production of about −6 %, due to the reduced wind speed in the wake of the first kite. We conclude that both the 6 % TI of the turbulent wind and the wake of the first kite are perturbations that are too small relative to the kite flight velocity to affect its tracking.

The investigations demonstrated the capability of the developed framework to perform simulations of kites in turbulent environments. We highlight the fact that kite wakes are intrinsically dependent on the kite trajectory and flight velocity and that, for the case of four-loop trajectories, the wake consists of discrete identifiable perturbations that can eventually interact strongly and merge, yet that remain of a limited longitudinal extent. This suggests that wake avoidance strategies and sophisticated control schemes could be

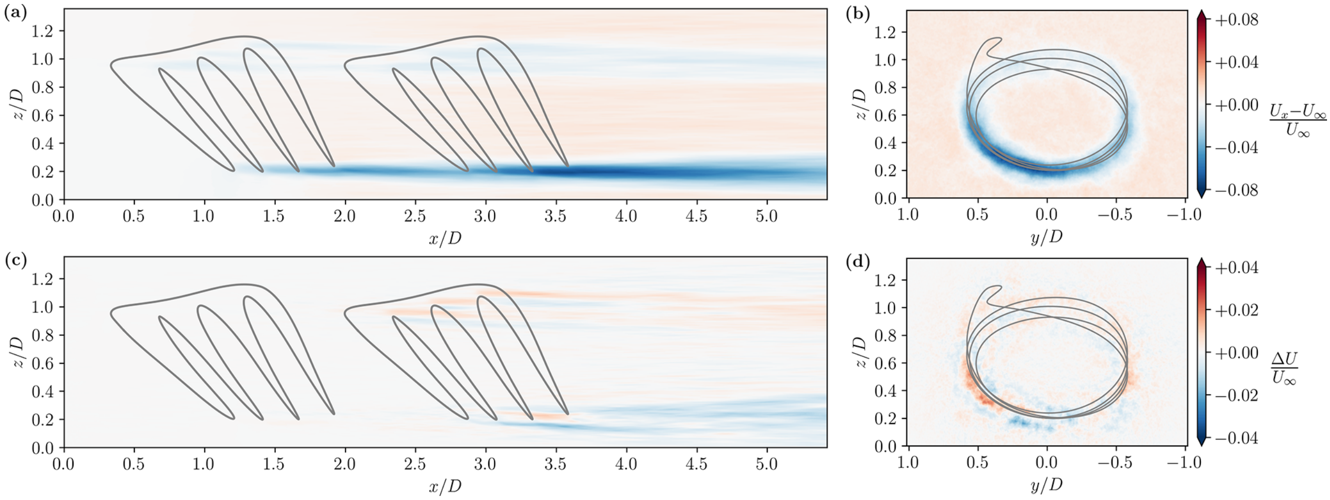

Figure 26. Six-cycle averaged streamwise velocity deficit of kites in tandem, where the second kite flies in-phase in a vertical longitudinal **(a)** and transversal plane at $4D$ from the inlet **(b)**; and difference in velocity ΔU caused by the trajectory phase shift on the second kite **(c, d)**.

developed to minimize the net power losses due to wakes for multiple kite configurations. In follow-up work, we aim at investigating kites flying in or through other kinds of strong perturbations, such as a kite also crossing the wake of a large conventional wind turbine during its trajectory. It should also be noted that assuming a uniform inflow affects the trajectory optimization and the wake behavior, compared to considering a sheared inflow. This aspect is therefore left for future investigation.

Appendix A: Kite geometry

Based on the MegAWES kite description in Eijkelhof and Schmehl (2022), the geometry of the kite considered in this work is further detailed. Some dimensions are adapted from Eijkelhof and Schmehl (2022). For example, the location and dimensions of the ailerons are corrected to coincide with the structural model obtained from the author. A detailed sketch of the adapted geometry is shown in Fig. A1.

The kite has a wingspan of 42.5 m and an aspect ratio of 12. The dash-dotted lines in Fig. A1 represent the control surface hinges. They coincide with the quarter chord for the elevator and the rudders. The widely spaced dashed line is the main wing quarter-chord line. Note that the aileron gaps were created solely to facilitate the overset mesh approach in the wing-resolved CFD of Pynaert et al. (2024), with whom we collaborate. When using the AL model, these gaps are replaced by the corresponding wing sections. A detailed description of the wing planform is provided in Table 4 of Eijkelhof and Schmehl (2022). However, within the BORNE project, the wing planform is slightly changed so that the final chord length and twist coincide with the data from Table 3 of the same reference. Here, we decide to assume linear chord and twist distributions.

The main wing chord is constant on the so-called root section, spanning from $-y_R$ to $+y_R$. Then it linearly decreases up to the tip from a chord length c_R to c_T. The point where the chord goes from constant to linear is chosen so that the planform surface keeps its area $S = 150.45\,\mathrm{m}^2$. The wing section is the RevE$_{\mathrm{HC}}$ aerodynamic profile (Eijkelhof, 2019). The two rudders and the elevator use a NACA0012 airfoil. The main wing is set at an angle of $-5°$ with respect to the aircraft x_0 axis and is linearly twisted from the end of the root section to the tip, where it reaches a $t_T = 5°$ twist angle. The constant section is chosen to be the same as for the chord. The chord of the tip aerodynamic profiles have therefore aligned (0° angle) with respect to the aircraft's x_0 axis. The angles of the wing sections are defined as positive for wash-out and negative for wash-in. The chord and twist distribution are therefore respectively

$$c(y) = \begin{cases} c_R & \text{if } y \leq y_R; \\ c_R + \frac{c_T - c_R}{y_T - y_R}(y - y_R) & \text{else,} \end{cases} \tag{A1}$$

and

$$t(y) = \begin{cases} t_R & \text{if } y \leq y_R; \\ t_R + \frac{t_T - t_R}{y_T - y_R}(y - y_R) & \text{else.} \end{cases} \tag{A2}$$

The value of y_R that maintains the right planform surface area is 4.65 m. The comparison between the reconstructed geometry and the data from Table 4 is shown in Fig. A2.

Furthermore, we also assume that the quarter-chord line is straight, as the relative error on the x distance to the front of the wing root is only 1.25 %. Also, the coordinates of the center of gravity in the x forward, y to port, and z downward reference frame are (−1.6729, 0.0, −0.2294). After discussion with the authors (Eijkelhof and Schmehl, 2022), it turns out that there was a typo in the z coordinate sign in the original publication.

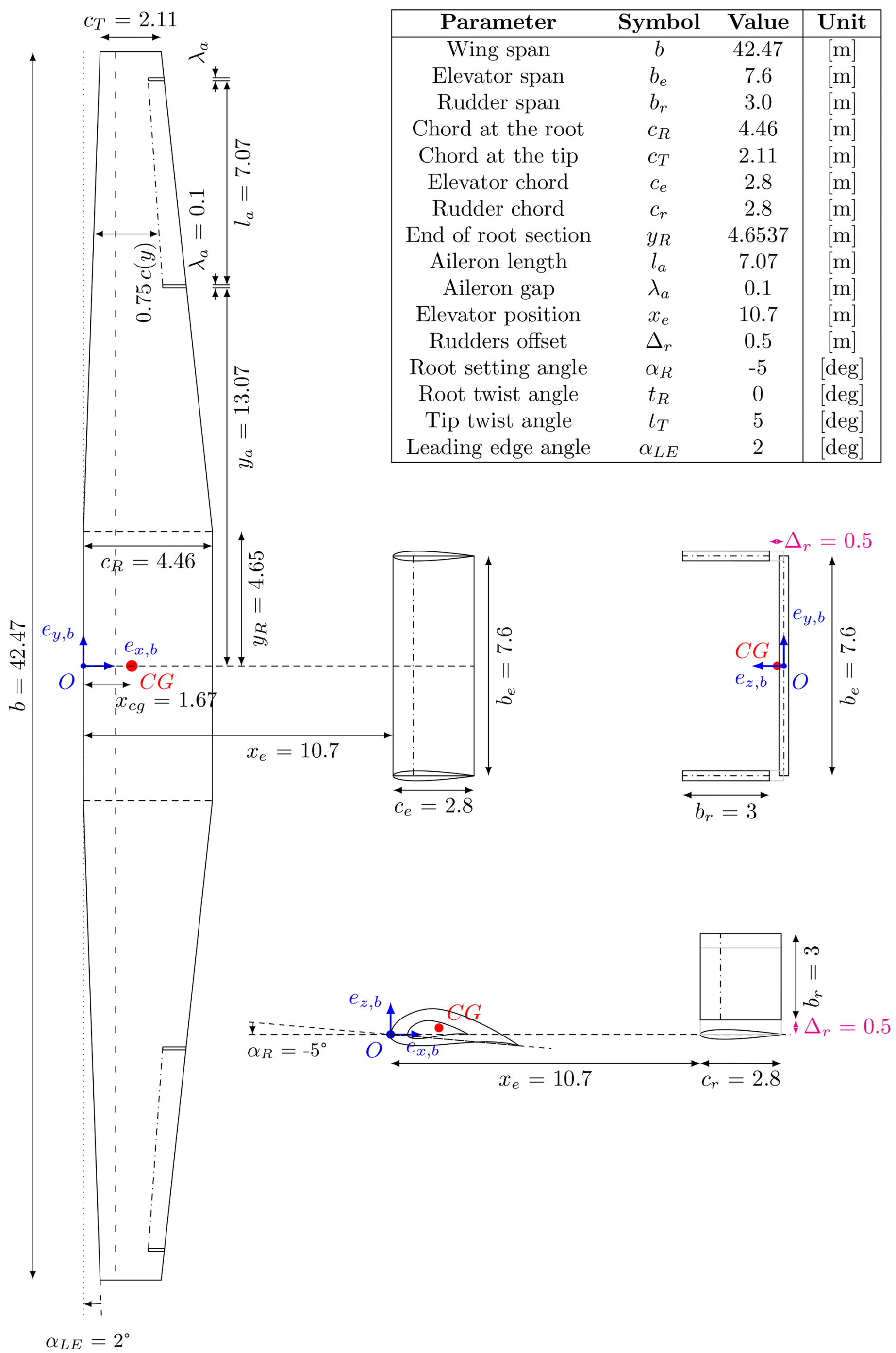

Parameter	Symbol	Value	Unit
Wing span	b	42.47	[m]
Elevator span	b_e	7.6	[m]
Rudder span	b_r	3.0	[m]
Chord at the root	c_R	4.46	[m]
Chord at the tip	c_T	2.11	[m]
Elevator chord	c_e	2.8	[m]
Rudder chord	c_r	2.8	[m]
End of root section	y_R	4.6537	[m]
Aileron length	l_a	7.07	[m]
Aileron gap	λ_a	0.1	[m]
Elevator position	x_e	10.7	[m]
Rudders offset	Δ_r	0.5	[m]
Root setting angle	α_R	-5	[deg]
Root twist angle	t_R	0	[deg]
Tip twist angle	t_T	5	[deg]
Leading edge angle	α_{LE}	2	[deg]

Figure A1. Top, port, and back view of the MegAWES aircraft with its main dimensions.

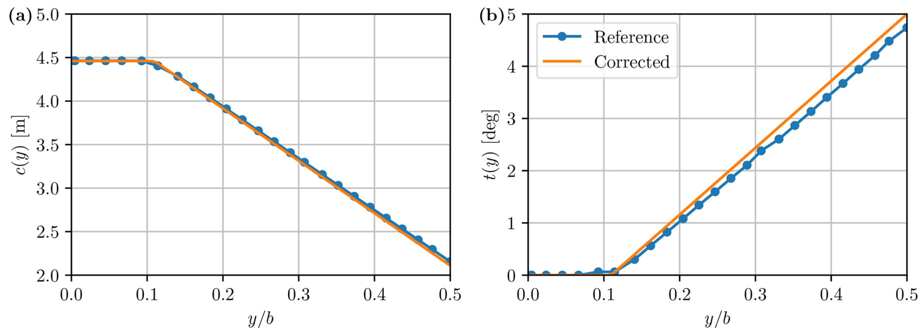

Figure A2. Comparison between the assumed chord **(a)** and twist **(b)** distribution data from Table 4 in Eijkelhof (2019).

Appendix B: Trajectory parameters

This Appendix gives the parameters used to generate the trajectory using AWEbox. The constraints on the states are given in Table B1, and the constraints on the control variables are provided in Table B2, along with some additional constraints, notably on important aerodynamic quantities. The OCP time horizon has been subdivided into 160 intervals (40 per loop). An additional parameter constraining the lower bound of the tether velocity during the reel-out phase is set to $-3.0\,\mathrm{m\,s^{-1}}$.

Table B1. Bound constraints applied to state variable $\boldsymbol{x}$ used in the optimal control problem. The maximal lateral extent of the flight path and the maximal tether length are respectively set to $y_{\max} = 225$ m and $l_{\max} = 1000$ m to limit the spatial footprint of the trajectories.

	Quantity Units	q_x [m]	q_y [m]	q_z [m]	ω_x [$^\circ\,\mathrm{s^{-1}}$]	ω_y [$^\circ\,\mathrm{s^{-1}}$]	ω_z [$^\circ\,\mathrm{s^{-1}}$]	δ_a [°]	$\delta_{e,r}$ [°]	l [m]	$\dot{l}$ [$\mathrm{m\,s^{-1}}$]
Generation	Min.	0.0	$-(y_{\max}+0.5b)$	$2b$	-10.0	-40.0	-25.0	-15.0	-7.5	0.0	-12.0
	Max.	$l_{\max}$	$+(y_{\max}-0.5b)$	$+\infty$	$+10.0$	$+40.0$	$+25.0$	$+15.0$	$+7.5$	$l_{\max}$	$+12.0$
Tracking	Min.	0.0	$-\infty$	$2b$	-50.0	-50.0	-50.0	-20.0	-10.0	0.0	-15.0
	Max.	$l_{\max}$	$+\infty$	$+\infty$	$+50.0$	$+50.0$	$+50.0$	$+20.0$	$+10.0$	$l_{\max}$	$+15.0$

Table B2. Bound constraints applied to control variable $\boldsymbol{u}$ and other variables used in the optimal control problem. The maximum tether tension is chosen as $T_{T,\max} = 1.7\mathrm{MN}$ as specified in Eijkelhof and Schmehl (2022).

	Quantity	$\dot{\boldsymbol{\delta}}$	$\ddot{l}$	T_T	$\ddot{\boldsymbol{q}}$	$\boldsymbol{v}_\mathrm{a}$	α	β	$P_{\max}$
	Units	[° s^{-1}]	[m s^{-2}]	[kN]	[g]	[m s^{-1}]	[°]	[°]	[MW]
Generation	Min.	−25.0	−2.5	0.0	−3.0	10	−12.0	−5.0	−2.5
	Max.	+25.0	+2.5	$T_{T,\max}$	+3.0	120	+4.0	+5.0	+2.5
Tracking	Min.	−50.0	−5.0	0.0	−4.0	10	−15.0	−10.0	−3.0
	Max.	+50.0	+5.0	$T_{T,\max}$	+4.0	120	+5.0	+10.0	+3.0

Appendix C: Stability derivatives

In the aerodynamic model described in Malz et al. (2019), the force coefficients are expressed as a superposition of different contributions from the angle of attack, side-slip angle, kite angular velocities, and control surfaces actuations, as described in Eqs. (11), (12a), and (12b). The sub-coefficients are evaluated for our AL-based model by imposing several movements to the kite in a simulation. The forces and moments are measured, and the sub-coefficients are obtained by inverting the model's equations. Such sub-coefficients are in fact second-order functions of the angle of attack α.

The LES framework allows one to impose the kite trajectory. A trajectory containing lateral motion, rotations in the three-body axis direction, and the actuation of the three sets of control surfaces at different angles of attack is constructed. Once all the different movements are performed, the angle of attack is increased. The different movements do not require the kite to actually move in the flow domain, but the velocities induced by the movements considered are taken into account by the AL method.

Table C1. Actuation magnitude used to evaluate the aerodynamic model coefficients.

Quantity	β	ω_x	ω_y	ω_z	δ_a	δ_e	δ_r
Units	[°]	[° s^{-1}]	[° s^{-1}]	[° s^{-1}]	[°]	[°]	[°]
Actuation	2.0	0.05	0.05	0.25	7.0	3.0	8.0

The simulation is performed in a domain of $6b \times 4b \times 4b$, and the aircraft is facing a uniform inflow of $100\,\mathrm{m\,s^{-1}}$, which is of the order of magnitude of the velocity at which the kite operates. The kite is thus placed $1.5b$ behind the inlet in the center of the domain and stays at that position for the whole simulation. Each movement is applied to the kite during 1 s, which corresponds to a flow displacement of about $2.5b$. Forces and moments are measured and averaged during the last 0.5 s, where the measurements are converged and steady. The forces and moments measured at a certain angle of attack, without any other actuations or movements, are then subtracted from the measurements taken during the different motions or actuations to evaluate the ad hoc coefficients. The magnitude of the movements and actuations are provided in Table C1. They are chosen such that they represent either the mean or the most encountered value along the trajectory.

The resulting coefficients are given in Table C2. It is to be noted that only the relevant terms are considered for each coefficient.

Table C2. Aerodynamic coefficients of the MegAWES aircraft as evaluated using the AL. The coefficients represents a second-order polynomial depending on α.

Coeff.	Term	a_0	a_1	a_2
C_X	0	−0.0406	+0.6091	+3.8723
	q	−0.5377	+2.5229	+5.8942
	δ_e	−0.0344	+0.3549	+0.2622
C_Y	β	−0.1763	−0.0019	+0.0955
	p	−0.0005	−0.0833	−0.3620
	r	+0.0744	−0.0089	−0.0368
	δ_a	+0.0014	−0.0066	−0.0166
	δ_r	+0.1762	+0.0047	−0.1778
C_Z	0	−0.9770	−4.0720	+6.2705
	q	−1.8502	−4.0302	−15.9874
	δ_e	−0.4516	+0.0922	+0.7698
C_l	β	−0.0074	+0.0009	+0.0153
	p	−0.5379	+1.6808	+8.1936
	r	+0.2211	+0.6395	+0.4973
	δ_a	−0.2415	−0.0879	−0.2742
	δ_r	+0.0073	+0.0000	−0.0050
C_m	0	+0.0618	−0.2795	−1.6016
	q	−6.7754	+0.4106	+3.1022
	δ_e	−1.2166	+0.0559	+0.9132
C_n	β	+0.0400	+0.0010	−0.0132
	p	−0.0830	−0.7384	+1.5599
	r	−0.0290	+0.0613	+0.0458
	δ_a	+0.0073	−0.1983	−0.0687
	δ_r	−0.0402	−0.0013	+0.0378

Code availability. The LES flow solver is a proprietary software of UCLouvain and is not publicly available. The toolbox `AWEbox` is openly accessible on GitHub (https://github.com/awebox, AWEbox, 2025). The presented simulation results are available upon request.

Data availability. The presented simulation results are available upon request.

Author contributions. JBC performed implementations in the LES flow solver and carried out the simulations. JBC analyzed the data with the insight of TH, MD, and GW. JBC wrote the paper. TH, MD, and GW revised the paper. The PhD work of JBC is supervised and advised by GW and MD.

Competing interests. The contact author has declared that none of the authors has any competing interests.

Disclaimer. Publisher's note: Copernicus Publications remains neutral with regard to jurisdictional claims made in the text, published maps, institutional affiliations, or any other geographical representation in this paper. The authors bear the ultimate responsibility for providing appropriate place names. Views expressed in the text are those of the authors and do not necessarily reflect the views of the publisher.

Acknowledgements. The present research benefited from computational resources made available on Lucia, the Tier-1 supercomputer of the Walloon Region, infrastructure funded by the Walloon Region under grant agreement no. 1910247.

We also thank Jochem De Schutter for his assistance with the toolbox `AWEbox`.

The authors used ChatGPT during paper preparation to improve text clarity and flow. All content was subsequently reviewed and edited by the authors, who take full responsibility for the publication.

Financial support. This work was conducted as part of the BORNE project, "Developing the tools and insight to expand the Belgian offshore wind farms with airborne wind energy systems", funded by the Energy Transition Fund of the Belgian Federal Public Service (FPS) Economy.

Review statement. This paper was edited by Roland Schmehl and reviewed by two anonymous referees.

References

Andersson, J. A. E., Gillis, J., Horn, G., Rawlings, J. B., and Diehl, M.: CasADi – a software framework for nonlinear optimization and optimal control, Mathematical Programming Computation, 11, 1–36, https://doi.org/10.1007/s12532-018-0139-4, 2019.

AWEbox: Modelling and optimal control of single- and multiple-kite systems for airborne wind energy, GitHub [code], https://github.com/awebox (last access: 6 July 2026), 2025.

Caprace, D.-G., Winckelmans, G., and Chatelain, P.: An immersed lifting and dragging line model for the vortex particle-mesh method, Theor. Comp. Fluid Dyn., 34, 21–48, https://doi.org/10.1007/s00162-019-00510-1, 2020.

Cocle, R., Bricteux, L., and Winckelmans, G.: Scale dependence and asymptotic very high Reynolds number spectral behavior of multiscale subgrid models, Phys. Fluids, 21, 085101, https://doi.org/10.1063/1.3194302, 2009.

Coquelet, M., Moens, M., Bricteux, L., Crismer, J.-B., and Chatelain, P.: Performance assessment of wake mitigation strategies, J. Phys. Conf. Ser., 2265, 032078, https://doi.org/10.1088/1742-6596/2265/3/032078, 2022.

Crismer, J.-B., Trigaux, F., Duponcheel, M., and Winckelmans, G.: Large-Eddy Simulation of airborne wind energy systems wakes, J. Phys. Conf. Ser., 2505, 012036, https://doi.org/10.1088/1742-6596/2505/1/012036, 2023.

Crismer, J.-B., Haas, T., Duponcheel, M., and Winckelmans, G.: Airborne wind energy systems flying optimal trajectories in turbulent wind using flight path tracking, J. Phys. Conf. Ser., 2767, 072021, https://doi.org/10.1088/1742-6596/2767/7/072021, 2024.

De Schutter, J., Leuthold, R., Bronnenmeyer, T., Malz, E., Gros, S., and Diehl, M.: AWEbox: an optimal control framework for single- and multi-aircraft airborne wind energy systems, Energies, 16, https://doi.org/10.3390/en16041900, 2023.

Dimitrov, N., Pedersen, M., and Hannesdóttir, Á.: An open-source Python-based tool for Mann turbulence generation with constraints and non-Gaussian capabilities, J. Phys. Conf. Ser., 2767, 052058, https://doi.org/10.1088/1742-6596/2767/5/052058, 2024.

Duponcheel, M., Bricteux, L., Manconi, M., Winckelmans, G., and Bartosiewicz, Y.: Assessment of RANS and improved near-wall modeling for forced convection at low Prandtl numbers based on LES up to $Re_\tau = 2000$, Int. J. Heat Mass Tran., 75, 470–482, https://doi.org/10.1016/j.ijheatmasstransfer.2014.03.080, 2014.

Eijkelhof, D.: Design and Optimisation Framework of a Multi-MW Airborne Wind Energy Reference System, Delft University of Technology & Technical University of Denmark, https://resolver.tudelft.nl/uuid:e759f9ad-ab67-43b3-97e0-75558ecf222d (last access: 6 July 2026), 2019.

Eijkelhof, D. and Schmehl, R.: Six-degrees-of-freedom simulation model for future multi-megawatt airborne wind energy systems, Renew. Energ., 196, 137–150, https://doi.org/10.1016/j.renene.2022.06.094, 2022.

Gros, S. and Diehl, M.: Modeling of Airborne Wind Energy Systems in Natural Coordinates, Springer Berlin Heidelberg, Berlin, Heidelberg, https://doi.org/10.1007/978-3-642-39965-7_10, 181–203, 2013.

Haas, T., De Schutter, J., Diehl, M., and Meyers, J.: Wake characteristics of pumping mode airborne wind energy systems, J. Phys. Conf. Ser., 1256, 012016, https://doi.org/10.1088/1742-6596/1256/1/012016, 2019.

Haas, T., De Schutter, J., Diehl, M., and Meyers, J.: Large-eddy simulation of airborne wind energy farms, Wind Energ. Sci., 7, 1093–1135, https://doi.org/10.5194/wes-7-1093-2022, 2022.

Hagen, L. v., Petrick, K., Wilhelm, S., and Schmehl, R.: Life-cycle assessment of a multi-megawatt airborne wind energy system, Energies, 16, https://doi.org/10.3390/en16041750, 2023.

Houska, B. and Diehl, M.: Optimal control for power generating kites, in: 2007 European Control Conference (ECC), https://doi.org/10.23919/ECC.2007.7068861, 3560–3567, 2007.

HSL: A collection of Fortran codes for large scale scientific computation, http://www.hsl.rl.ac.uk, last access: 6 July 2022.

IEA – International Energy Agency: Net Zero by 2050: A Roadmap for the Global Energy System, CC BY 4.0, Paris, https://doi.org/10.1787/c8328405-en 2021.

Jeanmart, H. and Winckelmans, G.: Investigation of eddy-viscosity models modified using discrete filters: a simplified "regularized variational multiscale model" and an "enhanced field model", Phys. Fluids, 19, 055110, https://doi.org/10.1063/1.2728935, 2007.

Joshi, R., Schmehl, R., and Kruijff, M.: Power curve modelling and scaling of fixed-wing ground-generation airborne wind energy systems, Wind Energ. Sci., 9, 2195–2215, https://doi.org/10.5194/wes-9-2195-2024, 2024.

Loyd, M. L.: Crosswind kite power (for large-scale wind power production), J. Energy, 4, 106–111, https://doi.org/10.2514/3.48021, 1980.

Malz, E., Koenemann, J., Sieberling, S., and Gros, S.: A reference model for airborne wind energy systems for optimization and control, Renew. Energ., 140, 1004–1011, https://doi.org/10.1016/j.renene.2019.03.111, 2019.

Mann, J.: The spatial structure of neutral atmospheric surface-layer turbulence, J. Fluid Mech., 273, 141–168, https://doi.org/10.1017/S0022112094001886, 1994.

McCormick, B.: Aerodynamics, Aeronautics, and Flight Mechanics, Wiley, ISBN 978-0-471-57506-1, 1995.

Moens, M. and Chatelain, P.: Correlations between wake phenomena and fatigue loads within large wind farms: a large-eddy simulation study, Frontiers in Energy Research, 10, https://doi.org/10.3389/fenrg.2022.881532, 2022.

Monaghan, J. J.: Extrapolating B splines for interpolation, J. Comput. Phys., 60, 253–262, https://doi.org/10.1016/0021-9991(85)90006-3, 1985.

Pynaert, N., Haas, T., Wauters, J., Crevecoeur, G., and Degroote, J.: Wing deformation of an airborne wind energy system in crosswind flight using high-fidelity fluid–structure interaction, Energies, 16, https://doi.org/10.3390/en16020602, 2023.

Pynaert, N., Haas, T., Wauters, J., Crevecoeur, G., and Degroote, J.: Moving control surfaces in a geometry-resolved CFD model of an airborne wind energy system, J. Phys. Conf. Ser., 2767, 022041, https://doi.org/10.1088/1742-6596/2767/2/022041, 2024.

Rapp, S., Schmehl, R., Oland, E., and Haas, T.: Cascaded pumping cycle control for rigid wing airborne wind energy systems, J. Guid. Control Dynam., 42, 2456–2473, https://doi.org/10.2514/1.G004246, 2019.

Sánchez-Arriaga, G., Pastor-Rodríguez, A., Sanjurjo-Rivo, M., and Schmehl, R.: A lagrangian flight simulator for airborne wind energy systems, Appl. Math. Model., 69, 665–684, https://doi.org/10.1016/j.apm.2018.12.016, 2019.

Sørensen, J. N. and Shen, W. Z.: Numerical modeling of wind turbine wakes, Journal of Fluids Engineering, 124, 393–399, https://doi.org/10.1115/1.1471361, 2002.

Trigaux, F., Moens, M., Chatelain, P., and Winckelmans, G.: Tilted wind turbines in farm configuration for improved global efficiency, J. Phys. Conf. Ser., 1618, 062035, https://doi.org/10.1088/1742-6596/1618/6/062035, 2020.

Trigaux, F., Chatelain, P., and Winckelmans, G.: Investigation of blade flexibility effects on the loads and wake of a 15 MW wind turbine using a flexible actuator line method, Wind Energ. Sci., 9, 1765–1789, https://doi.org/10.5194/wes-9-1765-2024, 2024a.

Trigaux, F., Villeneuve, T., Dumas, G., and Winckelmans, G.: Near-tip correction functions for the actuator line method to improve the predicted lift and drag distributions, J. Fluid Mech., 989, A1, https://doi.org/10.1017/jfm.2024.461, 2024b.

Vermillion, C., Cobb, M., Fagiano, L., Leuthold, R., Diehl, M., Smith, R. S., Wood, T. A., Rapp, S., Schmehl, R., Olinger, D., and Demetriou, M.: Electricity in the air: Insights from two decades of advanced control research and experimental flight testing of airborne wind energy systems, Annu. Rev. Control., 52, 330–357, https://doi.org/10.1016/j.arcontrol.2021.03.002, 2021.

Wächter, A. and Biegler, L. T.: On the implementation of an interior-point filter line-search algorithm for large-scale nonlinear programming, Math. Program., 106, 25–57, https://doi.org/10.1007/s10107-004-0559-y, 2006.

Zanon, M., Gros, S., and Diehl, M.: Model predictive control of rigid-airfoil airborne wind energy systems, in: Airborne Wind Energy, edited by: Ahrens, U., Diehl, M., and Schmehl, R., Chap. 12, Springer Berlin Heidelberg, Berlin, Heidelberg, https://doi.org/10.1007/978-3-642-39965-7_12, 219–233, 2013.